

Revising inelastic dark matter direct detection by including the cosmic ray acceleration

Jie-Cheng Feng,¹ Xian-Wei Kang,^{2,3,*} Chih-Ting Lu,⁴

Yue-Lin Sming Tsai,^{5,†} and Feng-Shou Zhang^{2,3}

¹*Department of Physics, Beijing Normal University, Beijing 100875, China*

²*Key Laboratory of Beam Technology of the Ministry of Education,*

College of Nuclear Science and Technology,

Beijing Normal University, Beijing 100875, China

³*Beijing Radiation Center, Beijing 100875, China*

⁴*School of Physics, KIAS, Seoul 130-722, Republic of Korea*

⁵*Key Laboratory of Dark Matter and Space Astronomy,*

Purple Mountain Observatory, Chinese Academy of Sciences, Nanjing 210033, China

(Dated: June 4, 2022)

Abstract

The null signal from collider and dark matter (DM) direct detector experiments makes the interaction between the DM and visible matter too tiny to reproduce the correct relic density for many thermal DM models. One of the most popular explanations is the inelastic DM scenario, allowing the coannihilation between two almost degenerated states in the dark sector. Unfortunately, the virialized DM component from the nearby halo is non-relativistic and not able to excite the DM ground state even if the relevant couplings can be considerable. Thus, the DM with either the light mass or large mass splitting can evade the traditional virialized DM searches. In this work, we connect the concept of cosmic-ray accelerated DM in our Milky Way (MW) and the direct detection of the inelastic scattering in the underground detectors to explore spectra that are resulted from several interaction types of the inelastic DM. We find that the mass splitting $\delta < \mathcal{O}(1 \text{ GeV})$ can still be reachable for the cosmic ray accelerated DM with mass range $1 \text{ MeV} < m_{\chi_1} < 100 \text{ GeV}$ and sub-GeV light mediator, by using the latest PandaX-4T data, even though we conservatively take the astrophysical parameter (effective length) $D_{\text{eff}} = 1 \text{ kpc}$.

* xwkang@bnu.edu.cn

† smingtsai@pmo.ac.cn

I. INTRODUCTION

The gravitational evidence of dark matter (DM) is rich and clear, but its non-gravitational interaction with the standard model (SM) has not yet been observed. On the other hand, if the DM number density in the early universe can be described by the thermal Boltzmann distribution like the SM particles, the PLANCK measured relic density [1] implies that DM must interact with the SM besides gravity. Among the various methods to detect the interaction between DM and SM, the laboratory measurements, including Large Hadron Collider (LHC) [2, 3] and DM direct detection (DD) [4, 5], provide the most robust searches. However, the null signals have been reported until now. Particularly, the limits from either XENON1T [4] or PandaX-4T [5] rule out the DM-proton elastic scattering cross section close to the neutrino floor. These stringent constraints squeeze the allowed DM model parameter space to some fine-tuning regions where the correct relic density is generated by some special mechanisms, for example, the resonance or coannihilation [6]. The coannihilation region indicates that the lightest DM particle χ_1 and the next lightest one χ_2 almost degenerate in mass. When the coannihilation mechanism governs the DM annihilations, it means that the $\chi_1 - \chi_1$ -SM coupling can be negligible. Consequently, the $\chi_1 - p$ elastic scattering will be suppressed [7–12]. On the contrary, the resonance region may be completely probed in the future DD sensitivities, e.g., see Higgs portal DM models [13–18].

The standard DM DD strategy is to detect the DM-nucleon interactions by measuring the recoil energy of the DM-nucleon scattering under the following consideration. When the Earth sweeps the local virialized halo, the Maxwell-Boltzmann distributed DM, hereafter called virialized DM (vDM), hits the detector target. Since the vDM velocity is non-relativistic, the currently measured nuclei recoil energy range does not cover DM mass lighter than ≈ 5 GeV for xenon-type detectors [4, 5, 19]. Furthermore, such a standard method may be also blind for searching the coannihilation region because the incoming vDM is non-relativistic and its small kinetic energy is not able to excite DM to the next lightest one even if the relevant coupling can be considerable. Quantitatively, one requires the DM mass heavier than $\mathcal{O}(\text{TeV})$ to detect an excitation from χ_1 to χ_2 with the mass splitting $\approx \mathcal{O}(100 \text{ keV})$ [20].

It has been proposed to search for accelerated vDMs by considering their collisions with the high energy cosmic ray (CR) protons [21–24]. Once the collisions, the DM mass below a

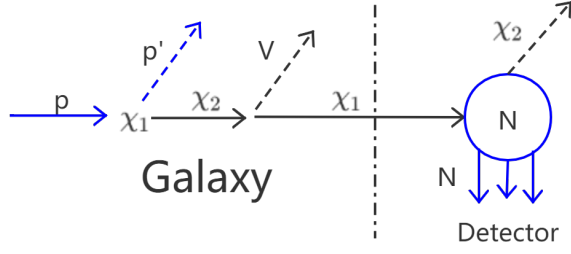


FIG. 1. Cosmic ray accelerated inelastic DM detection scenario: $p + \chi_1 \rightarrow p' + \chi_2 \rightarrow p' + \chi_1 + V$. Here p denotes the CR proton or helium, and the prime is used to distinguish the same particles in the initial and final states. The inelastic DM χ_1 and χ_2 are the ground state and excited state, respectively; V is the mediator between SM and DM; N is the target nucleus inside the underground detector. By this mechanism, the final χ_1 is accelerated.

few GeV can be accelerated to be relativistic and enter the underground detector with the kinetic energy higher than the designed threshold energy. This kind of cosmic ray accelerated vDM, called CRDM, recently received a lot of attention because it has a great performance on the present DM DD experiments. Even if the fluxes of CRDM are by several orders of magnitudes lower than vDM, the detection of CRDM helps us to probe the DM mass region lighter than a few GeV by using the sensitivity of XENONnT and PandaX-4T. This DM mass region was almost undetectable by using vDM scenario. With a similar idea, one can detect light CRDM by using the neutrino telescope [25] or study the diurnal effect caused by light CRDM [26]. In addition, such a collision between CR proton and DM may also smash the proton and produce neutrino and gamma ray [27].

We extend the CRDM elastic scattering to the inelastic scattering scenario, see the schematic cartoon in Fig. 1. The first vertex happens in the Milky Way where χ_1 is excited to χ_2 after the first collision. Unlike the elastic CRDM scenario, the χ_2 is not a stable particle and subsequently decays back to χ_1 and emits a mediator particle V before reaching the underground detector. Since we assume V in the decay is on-shell, we only focus on the light mediator situation in this study. The velocity of χ_1 here can be higher than elastic CRDM because the decay from heavier χ_2 can boost χ_1 again. The traditional vDM inelastic scattering search is limited to the heavier mass and low mass splitting [20]. Recently, investigating a similar scenario with the vector-vector interaction between fermionic DM and

SM, the authors have found that this approach can probe a larger mass splitting ≈ 100 MeV [28].

We notice that the DM-proton cross section of the vector-vector interaction is rather a constant independent with incoming proton energy. However, the CR spectrum rapidly decreases with CR energy. Except for the vector-vector interaction between fermionic DM and SM, there are more possible interaction types and the velocity dependent terms can be also important, which are beyond the popular (velocity-independent) spin-independent (SI) and spin-dependent (SD) form. Hence, we study several CRDM spectra based on different types of interactions to see the impact on the detected event rate. We investigate the exclusion power of the latest PandaX-4T data [5] in the region of the lower mass $m_{\chi_1} < 1$ GeV and larger mass splitting $\delta \sim \mathcal{O}(\text{GeV})$.

This paper is organized as follows. First, we introduce several different types of DM-SM interactions in Sec. II by considering both fermionic and scalar DM. In Sec. III, we elaborate the detection of the elastic and inelastic DM-proton scattering for both vDM and CRDM. In Sec. IV, we examine the interactions with the latest and most stringent exclusion from PandaX-4T. Finally, we conclude in Sec. V.

II. EFFECTIVE INELASTIC DM INTERACTIONS

To simply demonstrate our work, we hire some minimum DM Lagrangians where a Z_2 even vector/axial vector mediator V and a DM χ_1 with its excited state χ_2 are considered as the new implementation to the SM. We discuss both Majorana and real scalar DM fields in this study. The common nucleon- V interactions are

$$\mathcal{L}_{VN} = \bar{N}\gamma^\mu (C_N^v + C_N^a\gamma^5) NV_\mu. \quad (1)$$

The couplings C_N^v and C_N^a are for vector and axial vector interactions for nucleon. We require their sizes to be less than unity. Otherwise, the DM interaction with nucleon would be so strong and be observed by detectors already. The mediator V can be either photon-like boson charged under $U(1)$ gauge or Z -like boson charged under $SU(2)$ gauge. To maintain the gauge invariance, Ref. [29] suggests that if the boson V is $SU(2)$ dark Z , one shall compute the tree-level amplitude squared by using unitary gauge [30, 31]. Regardless of the gauge choice, for the vector interaction with $C_N^a = 0$, we find that its amplitude squared is

unaffected. On the contrary, the amplitude squared of the axial vector interaction ($C_N^v = 0$) can depend on our choice of gauge. Hereafter, we will simply take the unitary gauge and treat vector and axial vector interactions separately.

In what follows, we will discuss some interesting DM- V interactions \mathcal{L}_{VD} , and thus the completed Lagrangian to describe $p + \chi_1 \rightarrow p' + \chi_2$ process is $\mathcal{L}_{VN} + \mathcal{L}_{VD}$. After this section, we will only focus on some characteristic types of Lagrangian for demonstration.

A. Fermionic DM interaction

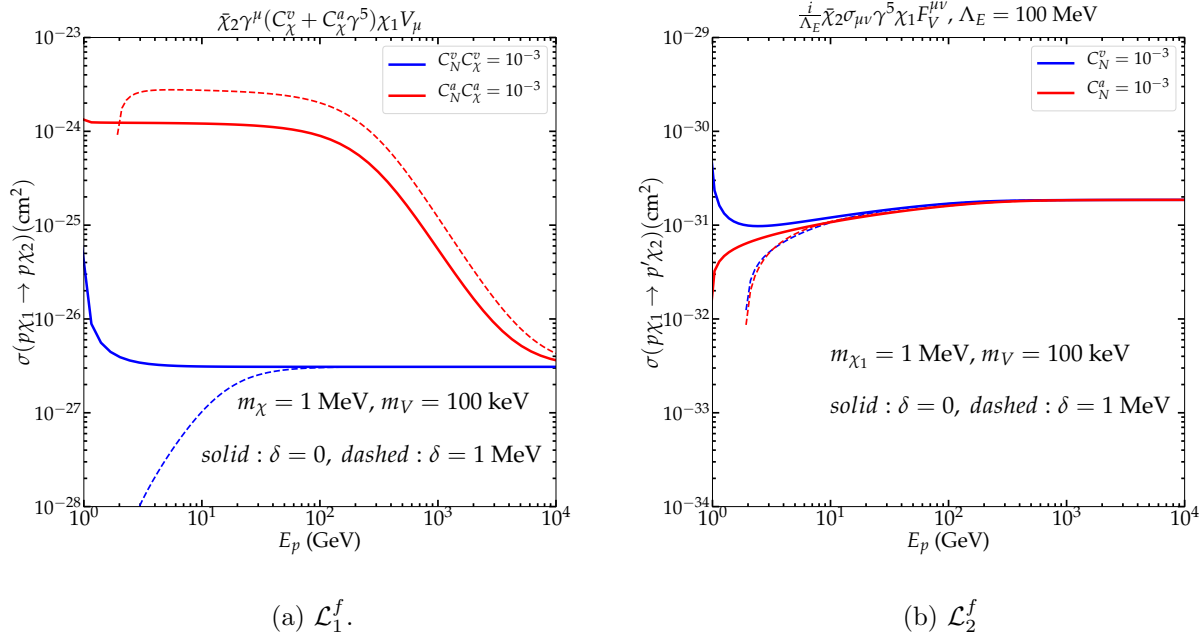


FIG. 2. The integrated cross section of process $p\chi_1 \rightarrow p'\chi_2$ as a function of incoming proton energy E_p . The AA interaction has a greater cross section than VV one while for \mathcal{L}_2^f , illustrated by ED, the resulting difference between the vector interaction and axial vector interaction of \mathcal{L}_{VN} is tiny.

For the fermionic DM scenario, we write down two common types of effective interactions between DM and V ,

$$\mathcal{L}_1^f = [\bar{\chi}_2 \gamma_\mu (C_\chi^v + C_\chi^a \gamma^5) \chi_1 + h.c.] V^\mu, \quad (2)$$

$$\mathcal{L}_2^f = \frac{1}{\Lambda_{E(M)}} \bar{\chi}_2 \sigma_{\mu\nu} \Gamma_{E(M)} \chi_1 F_V^{\mu\nu}, \quad (3)$$

where $F_V^{\mu\nu} = \partial^\mu V^\nu - \partial^\nu V^\mu$, $\sigma_{\mu\nu} = \frac{i}{2}(\gamma^\mu\gamma^\nu - \gamma^\nu\gamma^\mu)$, electric dipole-like interaction $\Gamma_E = i\gamma_5$, and magnetic dipole-like interaction $\Gamma_M = 1$. The index f refers to the Majorana DM. The parameter $\Lambda_{E(M)}$ is the new physics scale. It is a dimensional coupling that cannot be compared with C_χ^v or C_χ^a directly. Furthermore, we only concern with the product of $\chi\chi V$ and NNV couplings that appears in the scattering amplitude. Therefore, we can simply fix the coupling constants of the dark sector as constants $C_\chi^{v/a} = 1$ and $\Lambda_{E(M)} = 100$ MeV. We then compare the results based on different values of the NNV coupling, namely C_N^v or C_N^a , and one can rescale our result for other choices easily.

For simplicity, we focus on one type of interaction each time. In principle, there are four DM-SM interactions for \mathcal{L}_1^f : vector-vector (VV), vector-axial vector (VA), axial vector-vector (AV), and axial vector-axial vector (AA). Likewise, four possible DM-SM interactions for \mathcal{L}_2^f : vector-magnetic dipole (MD), axial vector-magnetic dipole, vector-electric dipole (ED), and axial vector-electric dipole. We will choose the representative operators VV, AA, ED, and MD in our work, based on the reasons that VV and AA interaction predicts the minimal and maximum $p - \chi_1$ cross sections, respectively, as well as that ED and MD are the most familiar DM models in the community.

The cross sections based on Eq. (2) and Eq. (3) are given in Appendix B2. For a comparison of axial vector and vector interaction in \mathcal{L}_{VN} , we present Fig. 2 for the integrated cross section of the process $p\chi_1 \rightarrow p'\chi_2$ as a function of incoming proton energy E_p for each interaction of \mathcal{L}_{VD}^f . The solid lines represent the degenerate scenario, namely, $m_{\chi_1} = m_{\chi_2}$ while the dashed lines are based on the inelastic cross section with $\delta = 1$ MeV. In Fig. 2a, the cross section of AA is higher than the one of VV at the lower E_p region. This is due to an additional contribution to the cross section of the AA, which dominates for small values of E_p . When the mediator mass is light, the enhancement is significant. The mass splitting can enhance axial vector interaction but suppress the vector interaction at the lower E_p region. However, at the large E_p region, all the interactions predict almost the same cross section. For dipole interactions of \mathcal{L}_{VD}^f , the resulting difference between vector and axial vector in \mathcal{L}_{VN} is less noticeable, as illustrated in Fig. 2b. One also notes that when the mass splitting δ exists, there is a kinematic constraint on E_p for the inelastic scattering. One can find more details in Appendix A. Therefore, the dashed lines do not start at $E_p = m_p$.

In Fig. 3, we show the integrated cross sections for \mathcal{L}_1^f (left panel) and \mathcal{L}_2^f (right panel) by comparing with three different mediator masses: $m_V = 10$ keV (blue lines), $m_V = 1$ MeV

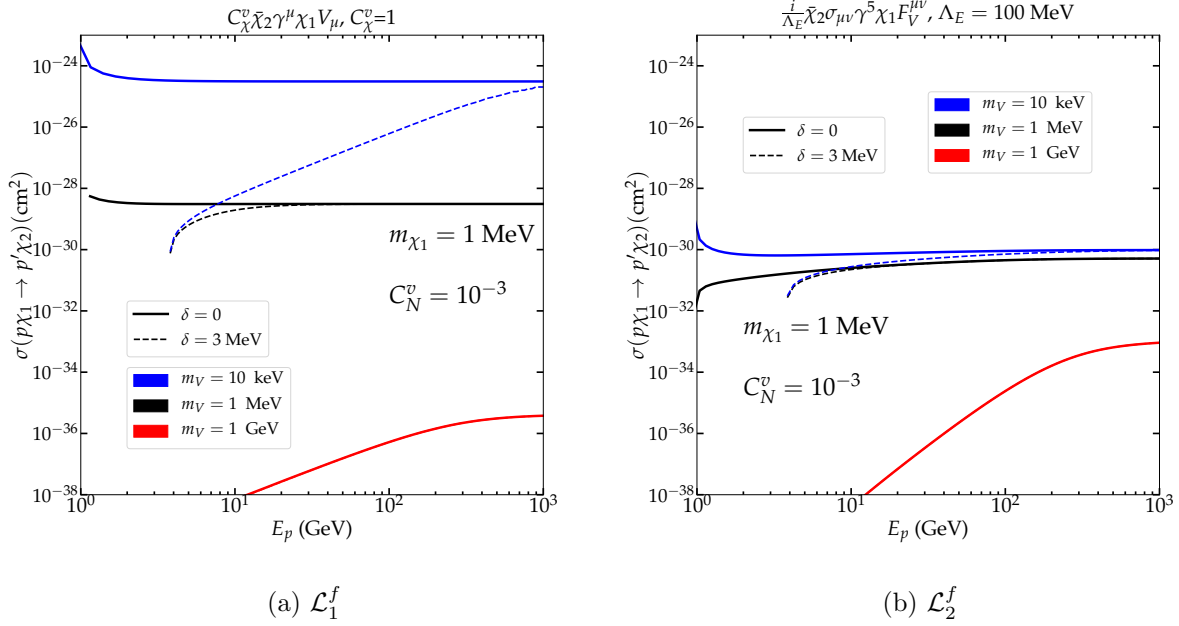


FIG. 3. The integrated cross section for the process $p\chi_1 \rightarrow p'\chi_2$ with respect to the energy of incoming proton E_p for \mathcal{L}_1^f (left panel) and \mathcal{L}_2^f (right panel). Three mediator masses 10 keV (blue lines), 1 MeV (black lines), and 1 GeV (red lines) are depicted. The difference between red dashed line and red solid line are negligible. We only plot the SM vector interaction ($C_N^a = 0$) case as a demonstration.

(black lines), and $m_V = 1$ GeV (red lines). Just for a demonstration, we only present the vector interaction (with $C_N^a = 0$) case while the cross section for the axial vector interaction will be larger as shown in Fig. 2. Again, we use the solid line for the degenerate scenario and the dashed line for the inelastic scattering. Generally speaking, both the larger δ and larger m_V can suppress the cross section at the small E_p region but the cross section will be saturated eventually at the high energy region. When $\delta \gg m_V$, the cross section can be even suppressed up to the $E_p > 100$ GeV region (cf. blue dashed line in pannel (a)). Comparing two different fermionic DM interactions, the suppression due to δ is rather severer in the \mathcal{L}_1^f than \mathcal{L}_2^f for the light m_V case.

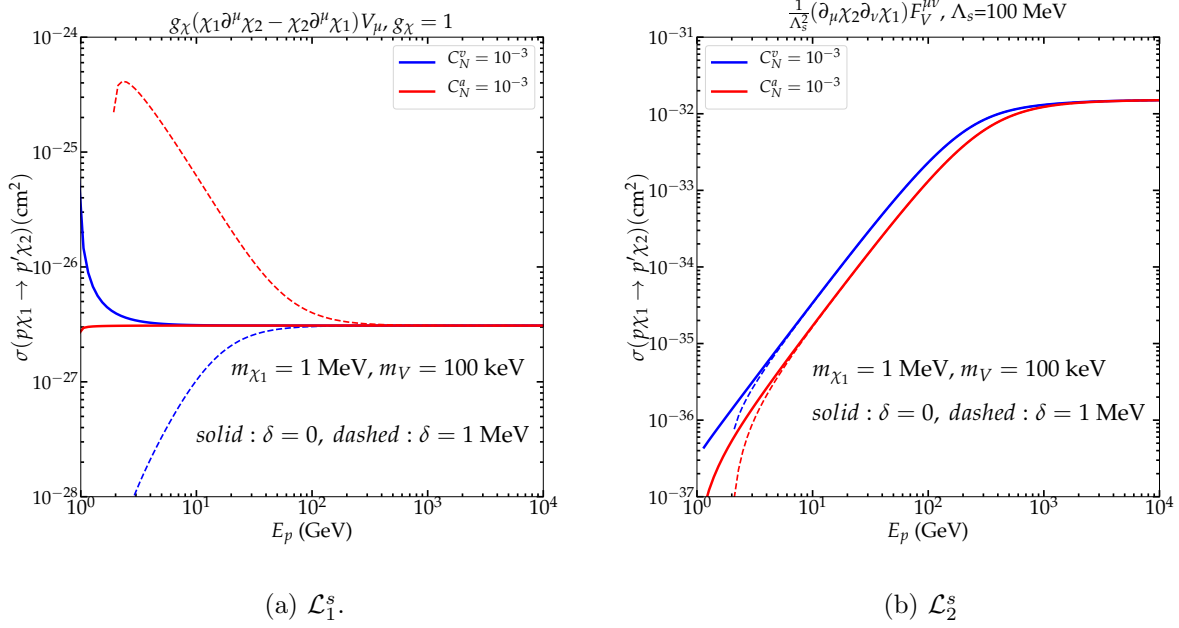


FIG. 4. The integrated cross section between scalar DM and an incoming proton as a function of its energy E_p . A non-zero δ contributes an enhancement for Lagrangian \mathcal{L}_1^s with SM axial vector interaction. For \mathcal{L}_2^s , the resulting difference between SM vector and axial vector interaction is tiny.

B. Scalar DM interaction

Regarding the interactions between the spin-zero inelastic scalar DM and the vector mediator, we also choose two benchmarks

$$\mathcal{L}_1^s = g_\chi(\chi_1 \partial^\mu \chi_2 - \chi_2 \partial^\mu \chi_1) V_\mu, \quad (4)$$

$$\mathcal{L}_2^s = \frac{1}{\Lambda_s^2} (\partial_\mu \chi_2 \partial_\nu \chi_1) F_V^{\mu\nu}. \quad (5)$$

As a comparison, the dipole-like interaction Eq. (5) is considered. The index s denotes scalar DM. As aforementioned, only the product of the DM and SM couplings appears in the cross section. We therefore only alter the SM coupling constant C_N^v and C_N^a in Eq. (2), and fix the coupling constants of the dark sector as $g_\chi = 1$ and $\Lambda_s = 100$ MeV.

In Fig. 4, we compare the integrated cross section for \mathcal{L}_1^s (left panel) and \mathcal{L}_2^s (right panel). The color scheme is the same as Fig. 2. Fixing the vector interaction of SM part, \mathcal{L}_1^s leads to almost identical cross section as the fermionic case \mathcal{L}_1^f by comparing the blue lines in Fig. 2a and 4a. This owes to the similarity of their amplitude squared structure. On the other hand, as for fixing the SM axial vector interaction, the $\delta = 0$ case for \mathcal{L}_1^s (red solid line) differs with

the one for \mathcal{L}_1^f , where the former is flat but an enhancement appears in the latter. This is due to the non-trivial behavior of amplitude squared of axial vector interaction with the unitary gauge. Meanwhile, for fixing the SM axial vector part we can observe that first, if increasing E_p to a sufficiently high value, both the DM interactions \mathcal{L}_1^f and \mathcal{L}_1^s lead to the cross sections with the same order using the same coupling strength; second, if we take $\delta = 0$ case, the enhancement for \mathcal{L}_1^s vanishes but it still remains for \mathcal{L}_1^f . Actually, this enhancement is only significant for a light mediator mass. For dipole form interaction \mathcal{L}_2^s as shown in Fig. 4b, the cross section is generally suppressed at the lower E_p region. In addition, the inelastic scattering cross section does not differ with elastic scattering one significantly.

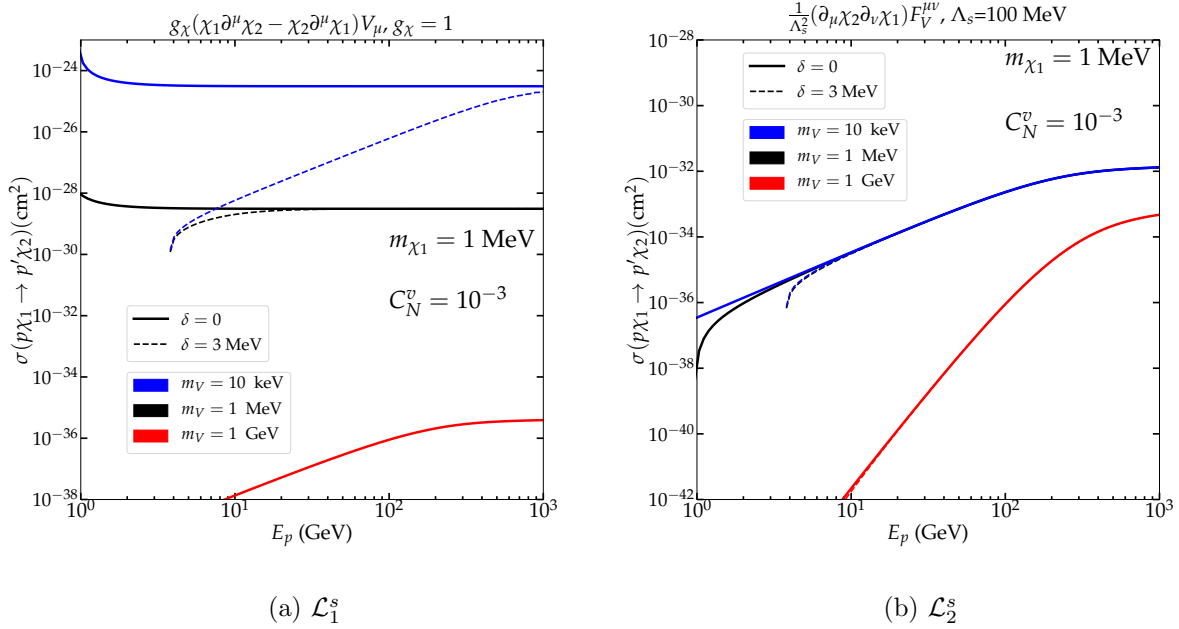


FIG. 5. Same as in Fig. 3 but for scalar DM scenario. The left and right panel are for the interaction \mathcal{L}_1^s and \mathcal{L}_2^s , respectively.

In Fig. 5, we plot the inelastic scalar DM scenario with the same scheme as in Fig. 3. As the similar amplitude squared structure, Fig. 3a and 5a are almost identical, even if their spins are different. For \mathcal{L}_2^s as shown in Fig. 5b, we can see that the cross section is not sensitive to δ at all. However, the cross section is sensitive to m_V only for large m_V (red lines) where its value is significantly suppressed.

III. THE DETECTION OF VDM AND CRDM

In this section, we first recap the formulas of traditional inelastic DM scattering with the target nuclei. Namely, vDM occupies around the Earth with the local density $\rho_0 = 0.3 \text{ GeV} \cdot \text{cm}^{-3}$ and its velocity distribution can be simply described by a soft truncated Maxwell-Boltzmann form. In the second part of this section, we the inelastic CRDM fluxes $d\phi_\chi/dT_\chi$ during the CR-DM collisions that can be altered with respect to different values of m_{χ_1} and δ . Finally, we estimate the detected inelastic DM event rate \mathcal{R} of the CRDM scattering with the target nuclei.

A. Traditional detection of the virialized DM

Let us first consider the case of vDM. The Earth sweeps the local DM halo where DMs are virialized and their velocity v can be well described by a Maxwell-Boltzmann distribution $f(v)$. Following the convention of Ref. [32], the differential event rate of scattering between DM and the target nucleus *per unit detector mass* with respect to the recoil energy Q can be written as

$$\frac{d\mathcal{R}}{dQ} = \sum_{\mathcal{T}} \xi_{\mathcal{T}} \frac{\rho_0}{m_{\chi_1} m_{\mathcal{T}}} \int_{v > v_{\min}(Q)} v f(v) \frac{d\sigma_{\chi\mathcal{T}}}{dQ} d^3v, \quad (6)$$

where the parameter $\xi_{\mathcal{T}}$ is defined as

$$\xi_{\mathcal{T}} = \frac{\eta_{\mathcal{T}} m_{\mathcal{T}}}{\sum_{\mathcal{T}} \eta_{\mathcal{T}} m_{\mathcal{T}}}, \quad (7)$$

and the isotope fraction $\eta_{\mathcal{T}}$ can be found in the website¹. The target mass $m_{\mathcal{T}}$ depends on the material used in the detectors. One shall not confuse the momentum transfer \mathbf{q} with the recoil energy Q and they are related by $\mathbf{q}^2 = 2m_{\mathcal{T}}Q$. For a mass splitting δ between χ_1 and χ_2 , the kinetic phase space in the inelastic process will be restricted by a minimum velocity (taking the limits of small δ and v)

$$v_{\min}(Q) = \frac{1}{\sqrt{2m_{\mathcal{T}}Q}} \left(\frac{m_{\mathcal{T}}Q}{\mu_{\chi N}} + \delta \right), \quad (8)$$

where $\mu_{\chi N}$ is the dark matter-nucleon reduced mass. By taking the non-relativistic limit $T_{\chi_1} = m_{\chi_1} v^2/2$ and one dimensional velocity distribution, one can see that Eq. (6) in terms

¹ <https://www.webelements.com/xenon/>

of the DM fluxes $d\phi_\chi/dT_\chi = \rho_0 f(v)/m_{\chi_1}^2$ returns the general form

$$\frac{d\mathcal{R}}{dQ} = \sum_{\mathcal{T}} \frac{\xi_{\mathcal{T}}}{m_{\mathcal{T}}} \int_{T_\chi[v_{\min}(Q)]} \frac{d\phi_\chi}{dT_\chi} \frac{d\sigma_{\chi\mathcal{T}}}{dQ} dT_\chi. \quad (9)$$

In the limit $v \rightarrow 0$, the cross section $d\sigma_{\chi\mathcal{T}}/dQ$ includes spin independent (SI) and spin dependent (SD) components. It is known that the SI component can be coherently enhanced by target atom number square \mathcal{A}^2 , namely

$$\frac{d\sigma_{\chi\mathcal{T}}^{\text{SI}}}{dQ} = \frac{d\sigma_{\chi p}^{\text{SI}}}{dQ} \times \frac{\mu_{\mathcal{A}}^2}{\mu_p^2} \times \left[\mathcal{Z} + \frac{f_n}{f_p} (\mathcal{A} - \mathcal{Z}) \right]^2 \times F^2(Q, \mathcal{A}, \mathcal{Z}), \quad (10)$$

where μ_p^2 and $\mu_{\mathcal{A}}^2$ is the DM-proton and DM-atom reduced mass, respectively, and for isospin conservation, $f_p = f_n$. When using a velocity- and spin-independent cross section in this work, we only take the Helm type form factor for $F^2(Q, \mathcal{A}, \mathcal{Z})$ as Ref. [33].

Finally, one can compare the theoretically predicted events with experimental measurement by including the efficiency of the underground detector $\epsilon(Q)$ to account for the experimental analysis. Hence, the total event rate is

$$\mathcal{R} = \int_0^\infty \epsilon(Q) \frac{d\mathcal{R}}{dQ} dQ. \quad (11)$$

B. Inelastic production of CRDM

The vDMs near the Earth are non-relativistic and their mean and escape velocity are around 240 km s^{-1} and 540 km s^{-1} . However, DM may be accelerated by high energy CR protons toward the Earth with a relativistic velocity. If the masses of χ_1 and χ_2 differ by a small mass splitting δ , such a high energy transfer from CR can excite χ_1 to χ_2 . The inelastic DM collision with CR proton can be described as

$$p + \chi_1 \rightarrow p' + \chi_2 \rightarrow p' + \chi_1 + V, \quad (12)$$

where p is a cosmic proton and V is a Z_2 even boson mediated between SM and dark sectors. To ensure that V is produced on shell, we require $\delta > m_V$ throughout this study. Comparing with the non-relativistic vDM originating from our neighborhood, the CRDM produced by $p\chi_1$ scattering may occur everywhere in our galaxy. Similar to Ref. [21, 22], the DM flux caused by $p\chi_1$ scattering is

$$\frac{d\phi_{\chi_1}^{\text{MW}}}{dT_{\chi_1}} = \int d\Omega \int_{\text{l.o.s.}} d\ell \int dE_p \frac{\rho_\chi(r)}{m_{\chi_1}} \frac{d\phi_p}{dE_p} \frac{d\sigma_{p\chi_1 \rightarrow p'\chi_1 V}}{dT_{\chi_1}}, \quad (13)$$

where we take the Navarro-Frenk-White halo profile for illustration and the DM halo density is defined as ρ_χ . The integration is performed along line of sight (l.o.s.). The distribution $d\sigma_{p\chi_1 \rightarrow p'\chi_1 V}/dT_{\chi_1}$ is to describe the differential cross section of the collision process given in Eq. (12) with respect to kinetic energy of the final state χ_1 . The differential flux of CR protons $d\phi_p/dE_p$ is in units of $\text{GeV}^{-1} \text{ cm}^{-2} \text{ s}^{-1} \text{ sr}^{-1}$.

In Ref. [27], they have compared two different CR proton spatial distributions: one with a uniform and isotropic distribution in a cylinder and the other one with the actual simulation resulting from GALPROP [34]. However, the differences of the accelerated DM fluxes between these two results are small. Therefore, we can follow Refs. [22, 24, 25, 27] to assume that the CR proton distribution is uniform and isotropic in a cylinder with radius $R = 10 \text{ kpc}$ and half-height $h = 1 \text{ kpc}$. The spectra for protons and helium are taken from Ref. [35] for $E_p \lesssim 10^6 \text{ GeV}$ (below the first knee). We can further take the CR fluxes approximately described by a broken power law $d\phi_p/dE_p \propto E_p^{-\gamma}$, where $\gamma \approx 3$ for $10^6 \lesssim E_p \lesssim 2 \times 10^8 \text{ GeV}$ (below the second knee), and $\gamma \approx 3.3$ for $2 \times 10^8 \lesssim E_p \lesssim 3 \times 10^9 \text{ GeV}$ (below the ankle). In addition, we simply neglect the $E_p > 3 \times 10^9 \text{ GeV}$ flux due to Greisen-Zatsepin-Kuzmin cutoff [36]. Since we only take the spatial independent $d\phi_p/dE_p$, we can simplify the standard DM fluxes Eq. (13) by integrating the DM halo density,

$$\frac{d\phi_{\chi_1}^{\text{MW}}}{dT_{\chi_1}} = \frac{\rho_0}{m_{\chi_1}} \times D_{\text{eff}} \times \sum_{i=p, \text{He}} \int dE_i \frac{d\phi_i}{dE_i} G_i^2(2m_{\chi_1} T_{\chi_1}) \frac{d\sigma_{p\chi_1 \rightarrow p'\chi_1 V}}{dT_{\chi_1}}, \quad (14)$$

where D_{eff} is effective length

$$D_{\text{eff}} = \int d\Omega \int_{\text{l.o.s.}} \frac{\rho[r(\ell, \Omega)]}{\rho_0} d\ell. \quad (15)$$

The $G_i^2(Q^2)$ here is simply taken as dipole form,

$$G_i^2(Q^2) = \left[1 + \frac{Q^2}{\Lambda_i^2} \right]^{-4}, \quad (16)$$

where $\Lambda_p = 770 \text{ MeV}$ and $\Lambda_{\text{He}} = 410 \text{ MeV}$ are taken into calculation.

Since the process in Eq. (12) is $2 \rightarrow 3$ process with on-shell produced χ_2 , one can simply take a narrow width approximation to break down the Feynman diagram to $p\chi_1 \rightarrow p'\chi_2$ and $\chi_2 \rightarrow \chi_1 V$. Therefore, the the distribution of cross section can be written as

$$\frac{d\sigma_{p\chi_1 \rightarrow p'\chi_1 V}}{dT_{\chi_1}} = \int \frac{d\sigma_{p\chi_1 \rightarrow p'\chi_2}}{dT_{\chi_2}} \frac{dT_{\chi_2}}{dT_{\chi_1}} \frac{dB_{\chi_2 \rightarrow \chi_1 V}}{d \cos \theta'} d \cos \theta', \quad (17)$$

where θ' is the angle between χ_2 direction in the lab frame of p_{χ_1} and χ_1 direction for $\chi_2 \rightarrow \chi_1 V$ decay in the χ_2 rest frame. The differential cross section $d\sigma_{p_{\chi_1} \rightarrow p'_{\chi_2}}/dT_{\chi_2}$ and expression of $dB_{\chi_2 \rightarrow \chi_1 V}$ are given in Appendix B.

Next, we need a Jacobian dT_{χ_2}/dT_{χ_1} . Considering the process of $\chi_2 \rightarrow \chi_1 + V$, we can express the final T_{χ_1} by initial E_{χ_2} in the lab frame,

$$T_{\chi_1} = \frac{E_{\chi_1}^* E_{\chi_2} + |\mathbf{p}_{\chi_1}^*| \sqrt{E_{\chi_2}^2 - m_{\chi_2}^2} \cos \theta'}{m_{\chi_2}} - m_{\chi_1}, \quad (18)$$

where $E_{\chi_1}^* = (m_{\chi_1}^2 + m_{\chi_2}^2 - m_V^2)/(2m_{\chi_2})$ and $|\mathbf{p}_{\chi_1}^*| = \sqrt{E_{\chi_1}^{*2} - m_{\chi_1}^2}$ are the energy and momentum of χ_1 in the χ_2 rest frame. By inverting Eq. (18), one can obtain the expression of T_{χ_2} as

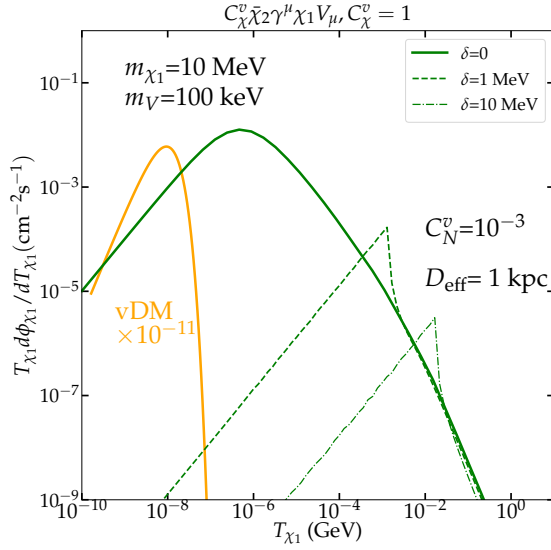
$$T_{\chi_2}(T_{\chi_1}, \cos \theta') = \frac{m_{\chi_2} E_{\chi_1}^* (m_{\chi_1} + T_{\chi_1})}{(E_{\chi_1}^*)^2 - (|\mathbf{p}_{\chi_1}^*| \cos \theta')^2} - m_{\chi_2} - \frac{m_{\chi_2} |\mathbf{p}_{\chi_1}^*| \cos \theta' \sqrt{(m_{\chi_1} + T_{\chi_1})^2 - (E_{\chi_1}^*)^2 + (|\mathbf{p}_{\chi_1}^*| \cos \theta')^2}}{(E_{\chi_1}^*)^2 - (|\mathbf{p}_{\chi_1}^*| \cos \theta')^2}. \quad (19)$$

We can differentiate the above equation to obtain dT_{χ_2}/dT_{χ_1} ,

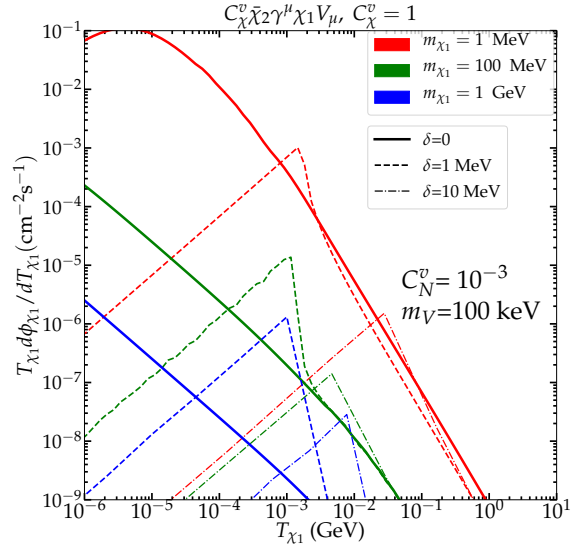
$$\frac{dT_{\chi_2}}{dT_{\chi_1}} = \frac{m_{\chi_2}}{(E_{\chi_1}^*)^2 - (|\mathbf{p}_{\chi_1}^*| \cos \theta')^2} \times \left[E_{\chi_1}^* - \frac{|\mathbf{p}_{\chi_1}^*| \cos \theta' (m_{\chi_1} + T_{\chi_1})}{\sqrt{(m_{\chi_1} + T_{\chi_1})^2 - (E_{\chi_1}^*)^2 + (|\mathbf{p}_{\chi_1}^*| \cos \theta')^2}} \right] \quad (20)$$

For illustration, we calculate the fluxes of several characteristic interactions by applying Eq. (17). Since the difference of SM axial vector and vector interaction has already been discussed (Fig. 2 and Fig. 4), we only display the situation of vector interaction and focus on the effects of kinematic variables. Also, we do not show the flux generated by \mathcal{L}_1^s from which the resulting cross section is similar to VV one.

In Fig. 6, we compare the vDM flux (orange solid line) with CRDM fluxes (green lines) by using $m_{\chi_1} = 10$ MeV, $m_V = 100$ keV, and $C_N^v = 10^{-3}$ (left). We use VV interaction for CRDM as demonstration, but the shapes for other interactions do not differ much except for their scales. For CRDM, we take $D_{\text{eff}} = 1$ kpc as a default value. The green solid line represents the elastic scattering with $m_{\chi_1} = m_{\chi_2}$ but the dashed and dash-dotted lines are with the mass splitting $\delta = 1$ MeV and $\delta = 10$ MeV, respectively. We note that a larger mass splitting makes a stronger suppression for the lower T_{χ_1} . We can clearly see that the fluxes of vDM in the Fig. 6a peaks at around 10^{-8} GeV where DM is with a non-relativistic velocity around $10^{-3}c$. As an expected feature from CRDM, its T_{χ_1} can be comparable with



(a) CRDM versus vDM .



(b) CRDM fluxes.

FIG. 6. (a) The comparison of vDM and CRDM fluxes. Both vDM and CRDM fluxes are obtained by using $\bar{\chi}_2 \gamma^\mu \chi_1 V_\mu$ interaction with $m_{\chi_1} = 10$ MeV, $m_V = 100$ keV, and $C_N^a = 10^{-3}$. The value of D_{eff} for CRDM is fixed to 1 kpc as a default value. (b) The spectra of CRDM with the VV interaction. Three benchmarks of DM mass 1 MeV (red lines), 100 MeV (greens lines), and 1 GeV (red lines) are presented. We also plot three different mass splittings, $\delta = 0$ (solid lines), $\delta = 1$ MeV (dashed lines), and $\delta = 10$ MeV (dash-dotted lines).

m_{χ_1} , where DM is relativistic particle. In fact, the light vDM, such as $m_{\chi_1} = 10$ MeV, is not detectable for present underground experiments, due to its tiny kinetic energy. However, both elastic and inelastic CRDM obtain enough energy to be observed. Moreover, we can see that the magnitude of fluxes of vDM can be around 11 orders higher than CRDM. This is because the integrated cross section of CR collision with DM is small ($\sim 10^{-27}$ cm²), even if the CRDM fluxes are accumulated over the line-of-sight, namely D_{eff} . It is impressive that the current powerful PandaX-4T and XENON1T detectors are capable to test such events.

Furthermore, we show the CRDM fluxes with three different DM masses and splittings in Fig. 6b. We adopt three benchmarks of DM mass 1 MeV (red lines), 100 MeV (greens lines), and 1 GeV (blue lines). For the three mass splittings, the solid, dashed, and dash-dotted lines correspond to the mass-degenerated case, $\delta = 1$ MeV, and $\delta = 10$ MeV, respectively. We can see that all the mass-degenerated cases are with smooth curves but those non-degenerated

curves show sharp peaks at T_{sp} . The spectrum follows the CR spectrum at the $T_\chi > T_{\text{sp}}$ region while it has a very different shape with CR one at the $T_\chi < T_{\text{sp}}$ region. As seen in Eq. (14), the CRDM energy spectrum is the product of the distribution $d\sigma_{p\chi_1}/dT_{\chi_1}$ and CR energy spectrum. We also learn from Figs. 2, 3, 4, and 5 that the cross section is flat at the high energy but δ contribution dominates $d\sigma_{p\chi_1}/dT_{\chi_1}$ at the lower energy region. Consequently, at the small energy region $T_\chi < T_{\text{sp}}$, the spectrum is strongly affected by $d\sigma_{p\chi_1 \rightarrow p'\chi_1 V}/dT_{\chi_1}$.

For the CRDM with $\delta = 0$, its energy is only provided by $p\chi_1$ elastic collision. Moreover, a final state χ_1 can be boosted by the δ owing to the χ_2 decay after the inelastic $p\chi_1 \rightarrow p'\chi_2$ process, as also mentioned in Ref. [28]. Therefore, the CRDM flux with a larger δ can depart from the mass-degenerate scenario toward to higher energy. *In sum, δ can cause a sharp peak T_{sp} in the spectrum toward the higher energy but with a decline of total flux.*

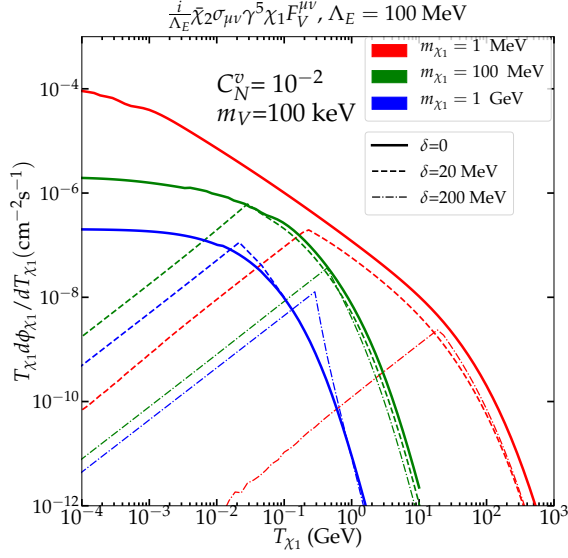
For dipole-like operators, we present the CRDM fluxes for fermionic DM cases (two upper panels) and scalar DM cases (two lower panels) in Fig. 7. The left panels show the light mediator scenarios ($m_V = 100$ keV) while the right panels show the heavy mediator scenario ($m_V = 10$ MeV). We use the same color scheme as Fig. 6b and the important features like the shifts of the shark peaks are also mentioned in the previous discussion. Comparing with the VV interaction in Fig. 6b, the spectra of the elastic scattering of all dipole-like interactions are softer. Therefore, the fluxes of the sharp peaks created by χ_2 decay ($\delta \neq 0$) are generally lower than $\delta = 0$ case in the dipole-like interactions. At last, the flux of scalar dipole-like DM interaction is lower than the fermionic one if using the same values of couplings. Note that $C_N^v = 10^{-1}$ for the former and $C_N^v = 10^{-2}$ for the latter.

C. The detection rate of CRDM

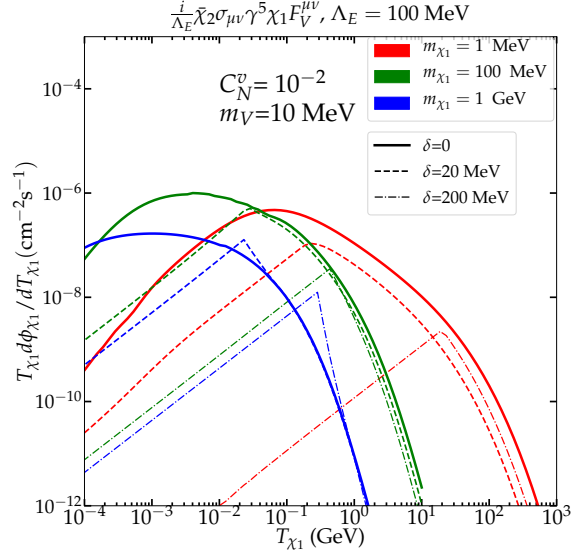
Following the conventions of Ref. [21, 37], we can write down the differential recoil rate per target nucleus of relativistic DM in underground detectors,

$$\frac{d\mathcal{R}}{dQ} = \sum_{\mathcal{T}} \frac{\xi_{\mathcal{T}}}{m_{\mathcal{T}}} \int_{T_{\text{min}}}^{\infty} dT_{\chi_1} \frac{d\sigma_{\chi_1 \mathcal{T}}}{dQ} \frac{d\Phi_{\chi_1}^{\text{MW}}}{dT_{\chi_1}}, \quad (21)$$

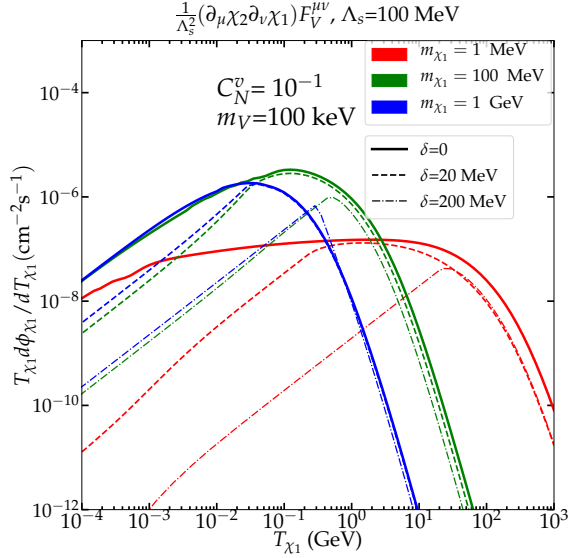
where T_{min} is the minimum kinetic energy of incoming DM and we only use $\mathcal{T} = \text{xenon}$ in this work. For those DM that strongly interact with nuclei, T_{min} can be varied with respect to the DM length of propagation in the Earth and the DM-nuclei cross section in



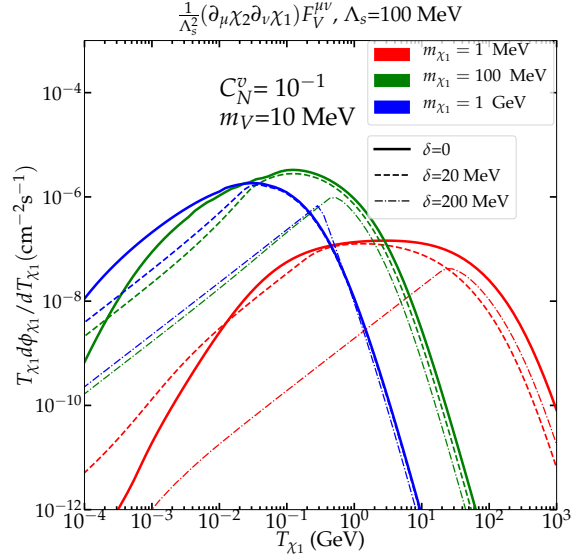
(a) Fermionic DM with $m_V = 100 \text{ keV}$.



(b) Fermionic DM with $m_V = 10 \text{ MeV}$.



(c) Scalar DM with $m_V = 100 \text{ keV}$.



(d) Scalar DM with $m_V = 10 \text{ MeV}$.

FIG. 7. The energy spectra of CRDM for \mathcal{L}_2^f (upper panels) and \mathcal{L}_2^s (lower panels). The mediator masses applied here are $m_V = 100 \text{ keV}$ (left figures) and $m_V = 10 \text{ MeV}$ (right figures). The color scheme is the same as Fig. 6b.

the attenuation process. Once the attenuation effect is not important, the T_{\min} only depends on the kinematics as shown in Appendix. A.

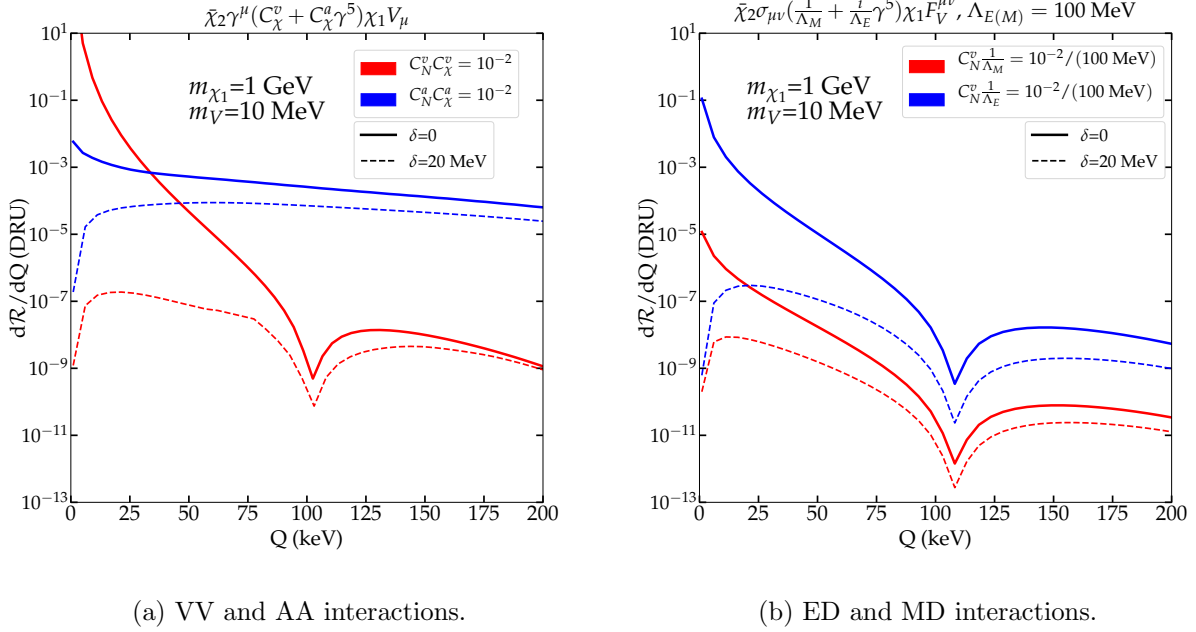


FIG. 8. The detection rate $d\mathcal{R}/dQ$ (DRU or $\text{keV}^{-1}\text{kg}^{-1}\text{day}^{-1}$) of fermionic CRDM χ -xenon scattering for \mathcal{L}_1^f (left) and \mathcal{L}_2^f (right). The mass degenerated cases $\delta = 0$ are represented as the solid lines while the dashed lines are for $\delta = 20$ MeV.

As presented in Sec. III A, the final $d\sigma_{\chi N}/dQ$ has to be the product of the χp cross section and the form factor as performing in Eq. (10). However, the form factor for SI or SD cross section is derived by a velocity independent technology. As shown in Ref. [38–42], a velocity dependent collision (e.g., dipole interaction) sometimes contains more than these two contributions. Therefore, we apply the effective operator method developed by Ref. [38–42] to exact the complete form factor for our inelastic interactions. In these works, the leading order of the velocity contribution is taken. Considering the fact that the form factor is to relate $\sigma_{\chi p}$ to $\sigma_{\chi T}$, the inelastic cross section of DM-target scattering is

$$\frac{d\sigma_{\chi T}}{dQ}(m_{\chi_1}, \delta, m_V, Q) = \left. \frac{d\sigma_{\chi T}}{dQ} \right|_{\text{EFT}} \times \frac{\mathcal{M}_{\chi p}^2(m_{\chi_1}, \delta, m_V, Q)}{\mathcal{M}_{\chi p, \text{EFT}}^2} \quad (22)$$

where the effective operator cross section $\left. \frac{d\sigma_{\chi T}}{dQ} \right|_{\text{EFT}}$ is obtained by using the public available numerical code LikeDM-DD [32]. For $\mathcal{M}_{\chi p}^2(m_{\chi_1}, \delta, m_V)$, we calculate them in the appendix B but $\mathcal{M}_{\chi p, \text{EFT}}^2$ is to take $\delta = 0$ and the limit $m_V \gg Q$. Owing to that the form factors are

independent of m_V and δ , Eq. (22) is valid. The VV, AA, MD, and ED interactions in effective theory limit are corresponding to the effective operators $\mathcal{Q}_1^{(6)}$, $\mathcal{Q}_4^{(6)}$, $\mathcal{Q}_1^{(5)}$, and $\mathcal{Q}_2^{(5)}$ in Ref. [32], respectively. Note that we here only present the fermionic DM cases because the result for scalar interaction \mathcal{L}_1^s is almost the same as VV one and \mathcal{L}_2^s is too suppressed by Λ_s^2 .

We show the predicted event rate with fermionic VV (red lines in Fig. 8a), AA (blue lines in Fig. 8a), MD (red lines in Fig. 8b), and ED (blue lines in Fig. 8b) interactions. We can clearly see a dip in the curves of VV, ED, and MD whose form factor contains a significant contribution from the SI component. The interaction AA may contain the SD component (without \mathcal{A}^2 enhancement) but the CRDM fluxes of AA interaction are generally higher than VV, so that the AA event rate is not so much lower than VV at the lower recoil range in elastic case. At the region $Q > 40$ keV, the spectrum of AA can be even higher than the one of VV by using the same parameters. Generally speaking in elastic case, the AA interaction predicts the highest event rate at the high Q but VV predicts the highest at the low Q . Due to the new physics scale $\Lambda_{E(M)}$ suppression, the dipole-like interactions ED and MD generally lead to lower rate. Furthermore the splitting δ can reduce the detected rate, and AA predicts the highest rate for $\delta = 20$ MeV. In other words, unlike elastic scattering scenario, the target xenon is more sensitive to detect the AA inelastic scattering cross section than the VV one, even if the AA interaction may not depend on the SI form factor enhanced by coherence.

Comments on the attenuation of the DM flux during the propagation: In this work, we simply ignore the attenuation effect from the Earth but focus on the exclusion limits as done in Ref. [28]. In principle, a simple version of transport equations should at least include the propagation of χ_1 and χ_2 . For the elastic CRDM scenario, the attenuation is important for $\sigma_{\chi p} > \mathcal{O}(10^{-28})$ cm² [21–25]. However, it is hard to know for inelastic scattering without a simulation. Considering the same cross section for both $\delta = 0$ and $\delta > 0$ scenarios, the inelastic DM can lose its energy much more efficiently than elastic DM because of $\chi_1 \rightarrow \chi_2$ excitation and χ_2 decay. On the other hand, if using the same coupling for these two scenarios, the cross section for $\delta > 0$ case maybe lower than the one for $\delta = 0$, such as for VV case.

Quantitatively, it would be deserved to develop a numerical code to simulate the energy distribution of χ_1 and χ_2 after their propagation, but it is beyond our current scope. We

are planning to return to this issue in the future with a designed numerical code.

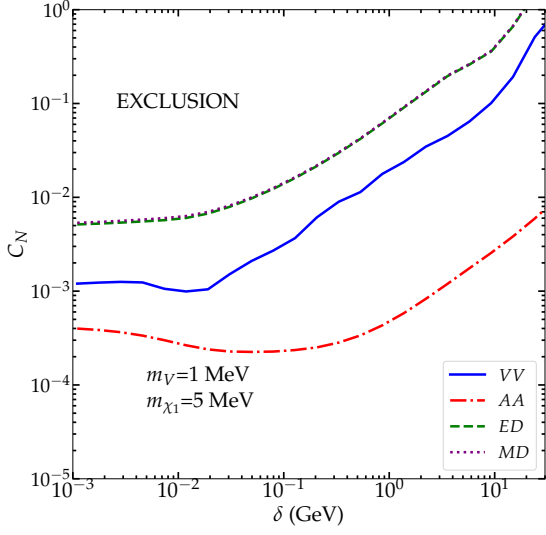
IV. CURRENT CONSTRAINTS FROM PANDAX-4T

The current most stringent limit of DM-proton scattering cross section is from PandaX-4T [5]. They have excluded the DM-proton elastic scattering cross section $\sigma_{\chi p}$ above $3.3 \times 10^{-47} \text{ cm}^2$ at DM mass $\sim 30 \text{ GeV}$ in 90% C.L. with 3.7-tonne of liquid xenon target and an exposure of 0.63 tonne \times year. However, such a limit is only for elastic vDM. To apply to inelastic and relativistic DM scenario, we have to restore the limit of event rate \mathcal{R} rather than the one of $\sigma_{\chi p}$.

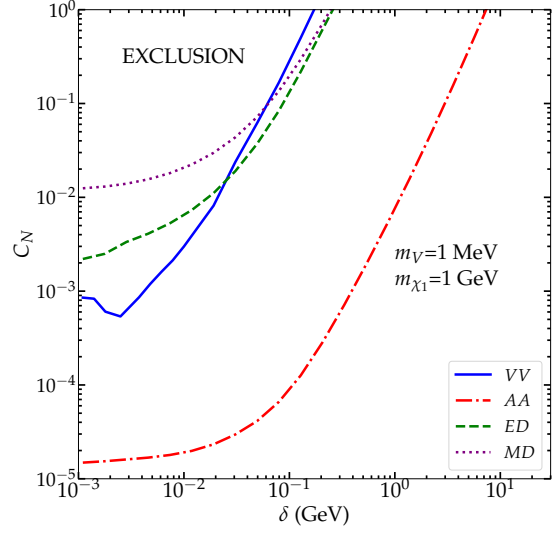
We just simply recast the PandaX-4T 90% C.L. of event rate in the following. First, we insert the published $\sigma_{\chi p}$ values of PandaX-4T 90% C.L. into Eq. (6) and Eq. (11), then the event rates for a fixed DM mass can be obtained. Actually, the published PandaX-4T exclusion plot is based on the recoil energy spectra which is related to the incoming DM kinetic energy. In this work, we simply take the efficiency curve from Ref. [43] and the window of the maximum efficiency is located for the detected recoil energies between 20 keV to 100 keV. Namely, we find the total event rate with the incoming DM momentum larger than threshold energy 30 MeV ($m_{\chi_1} = 30 \text{ GeV}$ with DM velocity $10^{-3}c$) is nearly a constant $\mathcal{R} \sim 4/0.63/\text{tonne}/\text{year}$. However, \mathcal{R} varies rapidly when the incoming DM momentum is smaller than 30 MeV. As a result, we use $\mathcal{R} \sim 4/0.63/\text{tonne}/\text{year}$ projected onto the (δ, C_N) and (m_{χ_1}, δ) planes to show the detection capability of PandaX-4T.

Our results are presented in Fig. 9. Generally, there are four unknown variables that we are interested in: m_{χ_1} , δ , m_V and the coupling strength $C_N = C_N^{a/v}$. Again, we take $D_{\text{eff}} = 1 \text{ kpc}$, $C_\chi^v = C_\chi^a = 1$, and $\Lambda_{E(M)} = 100 \text{ MeV}$ for dipole-like interaction here. As a reference, the $p\chi_1 \rightarrow p'\chi_2$ cross section with $C_N^{v/a} \approx 10^{-3}$ for VV and AA respectively, and $C_N^v \approx 10^{-2}$ for both MD and ED at a high E_p are approximately equal to $\mathcal{O}(10^{-28}) \text{ cm}^2$.

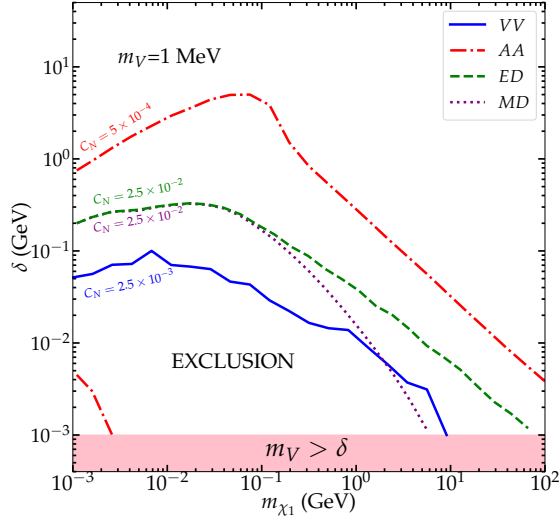
In Fig. 9a and 9b, by fixing m_{χ_1} and m_V , we obtain the limits of C_N for each δ and the VV (blue solid line), AA (red dash-dotted line), ED (green dashed line), and MD (purple dotted line) interactions. An interesting feature is that the exclusion lines of C_N remain relatively flat when the mass splitting is less than a certain level around $\delta \lesssim 10 \text{ MeV}$ here. *In other words, if δ is comparable to m_V , the total event rate is no longer sensitive to the changes of δ .* However, the δ larger than 10 MeV can weaken the limit. As mentioned in



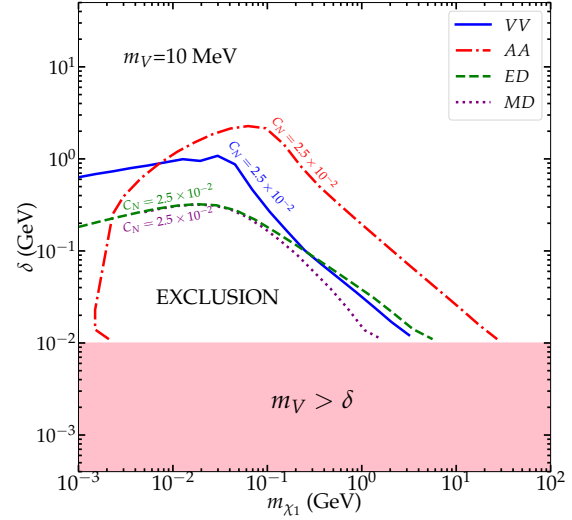
(a) $m_{\chi_1} = 5 \text{ MeV}$.



(b) $m_{\chi_1} = 1 \text{ GeV}$.



(c) $m_V = 1 \text{ MeV}$.



(d) $m_V = 10 \text{ MeV}$.

FIG. 9. The PandaX-4T limits projected onto the plane (δ, C_N) [two upper panels] and the plane (m_{χ_1}, δ) [two lower panels]. The line-of-sight halo integration D_{eff} is taken as 1 kpc. The benchmark interactions are VV (blue solid lines), AA (red dash-dotted line), ED (green dashed line), and MD (purple dotted line). In panel (a), ED and MD lines overlap. We fixed $\Lambda_{E(M)} = 100 \text{ MeV}$ for ED and MD.

the former sections, a larger δ can reduce the inelastic CRDM event rate. Comparing with the inelastic vDM scenario as the result from [20], the inelastic CRDM helps us to probe a larger δ region. When increasing m_{χ_1} , the limits for the interactions with a γ^5 (AA and ED) at the region $\delta < 10^{-2}$ GeV are significantly improved, but the limit for the MD interaction can be even weaker. At the large δ region, PandaX-4T rapidly loses the exclusion power if considering a large m_{χ_1} . Since the order of coupling strength can also represent the related size of DM-proton cross section, the PandaX-4T result projected on the AA interaction can give a most stringent limit on C_N while the higher dimensional operators, especially MD, have weaker limits.

Fig. 9c and 9d show the exclusion limits from PandaX-4T projected to (m_{χ_1}, δ) plane. Due to the on-shell condition $\delta > m_V$, the pink region is not accessible. Based on the information of Fig. 9a and 9b, we arbitrarily fix their couplings in order to optimize their detection as closer as the PandaX-4T limit at $\delta \rightarrow 0$. In Fig. 9c, we find that only the exclusion region of AA interaction is between two red dash-dotted lines, while the exclusion regions are below the corresponding lines for other interactions. This is because the mass splitting (see Fig. 2a as well) plays a role of enhancement in AA interaction. In the left bottom corner with $\delta < 5 \times 10^{-2}$ GeV and $m_{\chi_1} < 2 \times 10^{-3}$ GeV, it becomes an allowed region again for AA interaction. Of course, as long as we choose some stronger coupling, this allowed region can sink to the inaccessible (pink) region. In Fig. 9d, we take all the coupling strength $C_N = 2.5 \times 10^{-2}$. One can see that a turning point appears in all the interactions and the limits behave differently at the smaller and larger m_{χ_1} regions. We can understand them as the following. The upper limits of δ at the large m_{χ_1} region is decreasing with respect to m_{χ_1} , mainly because DM number density ρ_0/m_{χ_1} is decreasing. The limits at the small m_{χ_1} region are similar with vDM ones which always increase with m_{χ_1} . With a heavy mediator mass $m_V = 10$ MeV and $C_N = 2.5 \times 10^{-2}$, we find that PandaX-4T provides the most stringent limit for AA at large m_{χ_1} region but for VV at the lower m_{χ_1} region. With a help of CRDM scenario, the PandaX-4T exclusion of δ can be extended to 0.1 GeV, even 1 GeV in some cases.

V. CONCLUSION AND PROSPECT

In this work, we are motivated by the feature that DM relic density can be simply fulfilled at the co-annihilation region but DM located at this region escapes from the standard DM direct detection constraints. Therefore, we perform a study of the inelastic DM models which contain a pair of almost mass-degenerated DM particles χ_1 and χ_2 . Since the standard DD method is not able to detect the vDM with the extremely low momentum, this kind of inelastic DM model can be hidden within the analysis unless the DM mass is heavy enough $m_{\chi_1} \sim \mathcal{O}(\text{TeV})$. By considering the relativistic CRDM events created by the collision between the non-relativistic vDM with the CR proton and Helium, the lightest χ_1 can be excited to χ_2 and successively decay back to χ_1 . The very energetic χ_1 can be detected within the DM underground detector such as PandaX-4T in this study. *We have demonstrated that the mass splitting $\delta < \mathcal{O}(1 \text{ GeV})$ can still be reachable for the DM mass range considered in this work, by using the latest PandaX-4T data, even though we conservatively take the astrophysical parameter $D_{\text{eff}} = 1 \text{ kpc}$.*

Recently, a similar work [28] has been performed with the VV interaction resulting in a rather flat cross section with respect to the CR proton energy E_p . Beyond the scope of Ref. [28], we further study several different interactions including both fermionic and scalar DM. By studying the predicted CRDM spectra of the different interactions, we have found that the parameters (m_{χ_1} , δ , m_V , and E_p) play very different roles in the fermionic AA interactions of Eq. (2) compared with others, while the fermionic VV interaction of Eq. (2) is almost identical with the scalar interaction of Eq. (4). On the other hand, we have also studied the dimension-suppressed dipole-like interactions of Eq. (3) and Eq. (5). Since the χ_1 can be relativistic before colliding with xenon in the detectors, we adopt the velocity-dependent form factor based on the effective theory framework. Therefore, our results for the AA and dipole-like interactions can be more reliable.

We then comment on possible constraints from other experiments which may be able to test the same parameter space. On one hand, we focus on the mass of mediator m_V smaller than δ and m_{χ_1} in our study. On the other hand, we assume that the mediator is leptophobic. With these two conditions, the cross sections of DM productions via off-shell mediator in fixed target, B-factories, and LHC experiments are suppressed. Therefore, if $C_N \lesssim 10^{-2}$,

we can safely ignore the above constraints in our scenarios². However, the light leptophobic mediator is confronted with the constraints of the low energy n-Pb scattering [44, 45] and hadronic $\Upsilon(1S)$ decay [49]. Especially, the former one provides the constraint $C_N \lesssim 5 \times 10^{-3}$ for $m_V \lesssim 10 \text{ MeV}$ [50] but it loses the exclusion power once the m_V is increasing. We find that the upper limit of C_N from the low energy n-Pb scattering can be complemented to the PandaX-4T limit derived in this work.

In the last paragraph, we would like to point out several interesting extensions of this work, though they are beyond the scope of this paper. The first interesting follow-up work will be concerning the Earth attenuation effect of the CRDM propagation. In this work, we only focus on the exclusion limit but the attenuation can be important when the χ_{1p} interaction cross section is large. Comparing with the scenario for elastic CRDM scattering with Earth atoms, the inelastic scattering requires two dark particle propagation equations. In addition, the geometry of the propagation region might be complicated and it can be challenging to solve the propagation equations analytically. Hence, we will return to this issue in the future with a numerical solution. The second interesting work is to elaborate the form factor more precisely. In this work, we just simply re-scaled the form factor obtained by the assumption of elastic scattering. In addition, only the leading order of the velocity contribution has been included. Albeit tons of effort may need, it can be a useful work to develop a more realistic form factor for inelastic scattering.

ACKNOWLEDGMENTS

We would like to thank Jianglai Liu for the PandaX-4T efficiency table; thank Qian Yue and Jin Li for discussions on the experimental issues; thank Gang Guo and Shao-Feng Ge for their valuable comments. This work is supported by the National Natural Science Foundation of China under Grant No. 11805012 and No. 12135004; by the KIAS Individual Grant No. PG075302 at Korea Institute for Advanced Study.

² Note that this mass spectrum setting is different from the usual ones with $m_V > 2m_{\chi_1} + \delta$ in Ref. [46–48].

Appendix A: Kinematics of Two-body Inelastic collisions

As schematically depicted in Fig. 1, there are two scenarios of the DM collisions: (i) the high-energy protons of cosmic rays scattering with stationary DM χ , namely $p + \chi_1 \rightarrow p' + \chi_2$, where χ_2 is the excited state of χ_1 with a mass of $m_{\chi_2} = m_{\chi_1} + \delta$; (ii) the accelerated DM colliding with the stationary nucleus N in the detector $\chi_1 + N \rightarrow \chi_2 + N'$.

Considering the general two-body relativistic collision, $p_1 + p_2 \rightarrow p_3 + p_4$, their masses are m_i with $i = 1, 2, 3, 4$. We can write down the 4-momentum of each particle of the process in lab frame Σ^L :

$$\begin{aligned} p_1 &= (E_1, \mathbf{p}_1), \\ p_2 &= (E_2 = m_2, \mathbf{p}_2 \simeq 0), \\ p_3 &= (E_3, \mathbf{p}_3), \\ p_4 &= (E_4, \mathbf{p}_4). \end{aligned} \tag{A1}$$

While in the center-of-mass (CM) frame Σ^* , all physical quantities are marked with $*$:

$$\begin{aligned} p_1^* &= (E_1^*, \mathbf{p}_1^*), \\ p_2^* &= (E_2^*, \mathbf{p}_2^* = -\mathbf{p}_1^*), \\ p_3^* &= (E_3^*, \mathbf{p}_3^*), \\ p_4^* &= (E_4^*, \mathbf{p}_4^* = -\mathbf{p}_3^*), \end{aligned} \tag{A2}$$

The total 4-momentum P of two systems are simply

$$P(\Sigma^*) = (M, 0), \quad \text{and} \quad P(\Sigma^L) = (E_1 + m_2, \mathbf{p}_1). \tag{A3}$$

One also has

$$\begin{aligned} |\mathbf{p}_3^*| &= \frac{1}{2} \sqrt{\frac{(m_3^2 - m_4^2)^2}{M^2} + M^2 - 2(m_3^2 + m_4^2)}, \quad \text{and} \\ E_4^* &= \frac{M^2 - m_3^2 + m_4^2}{2M}. \end{aligned} \tag{A4}$$

Boosting from CM frame to lab frame, one will get the magnitude of velocity $\beta = |\mathbf{p}_1| / (E_1 + m_2)$ and Lorentz factor $\gamma = (E_1 + m_2) / M$. Therefore, the invariant mass M will be related to E_1 via

$$M = (E_1 + m_2) \sqrt{1 - \beta^2} = \sqrt{m_2^2 + m_1^2 + 2m_2 E_1}. \tag{A5}$$

1. The accelerating process $p + \chi_1 \rightarrow p' + \chi_2$

In the process of $p(p_1) + \chi_1(p_2) \rightarrow p'(p_3) + \chi_2(p_4)$, where the four-momentum label has been given in the parenthesis, one has $p_2 = (E_2 = m_{\chi_1}, \mathbf{p}_2 \simeq 0)$, and χ_2 is the accelerated DM after collision, with energy E_4 . We can insert $E_1 = E_p$, $m_1 = m_3 = m_p$, $m_2 = m_{\chi_1}$, and $m_4 = m_{\chi_1} + \delta$ into Eq. (A4) and obtain

$$E_4^* = E_{\chi_2}^* = \frac{m_{\chi_1}(m_{\chi_1} + E_p) + \delta(\delta/2 + m_{\chi_1})}{M}. \quad (\text{A6})$$

If $\delta = 0$, we can safely return to the case of elastic collision. Furthermore, the condition $E_{\chi_2}^* > (m_{\chi_1} + \delta)$ is required for χ_1 being excited to χ_2 . It results in an universal lower limit for E_p , which is $m_p + \delta + \frac{\delta(\delta+2m_p)}{2m_{\chi_1}}$.

In order to figure out the minimum value of E_p in Eq. (14), it would be useful to introduce the scattering angle θ^* where the component of \mathbf{p}_3^* along the direction of \mathbf{p}_1^* is $|\mathbf{p}_3^*| \cos \theta^*$. Therefore, we substitute E_4 by $T_{\chi_2} + m_{\chi_1} + \delta$ to obtain

$$T_{\chi_2} = \frac{E_{\chi_2}^*(m_{\chi_1} + E_p) - |\mathbf{p}_{\chi_2}^*| \sqrt{E_p^2 - m_p^2} \cos \theta^*}{\sqrt{(m_{\chi_1} + m_p)^2 + 2m_{\chi_1}(E_p - m_p)}} - (m_{\chi_1} + \delta). \quad (\text{A7})$$

where $|\mathbf{p}_{\chi_2}^*| = \sqrt{(E_{\chi_2}^*)^2 - (m_{\chi_1} + \delta)^2}$.

We would like to obtain the range of E_p from Eq. (A7). Since one can see that $T_{\chi_2}(E_p, \cos \theta^*)$ reaches maximum and minimum value when $\theta^* = \pi$ and $\theta^* = 0$ respectively, we may define $T_{\chi_2}^{\max}(E_p) = T_{\chi_2}(E_p, \theta^* = \pi)$ and $T_{\chi_2}^{\min}(E_p) = T_{\chi_2}(E_p, \theta^* = 0)$. For a fixed E_p , the allowed region of T_{χ_2} should be between $T_{\chi_2}^{\min}$ and $T_{\chi_2}^{\max}$, illustrated in Fig. 10.

Similar as the elastic case, the constraint of T_{χ_2} can be expressed by $E_p^{\min}(T_{\chi_2})$:

$$E_p > E_p^{\min} = \frac{T_{\chi_2} + \delta}{2} + \sqrt{\frac{T_{\chi_2}(m_{\chi_1} + \frac{T_{\chi_2}}{2} + \delta)(2m_p^2 + m_{\chi_1}T_{\chi_2} - \frac{\delta^2}{2})}{2m_{\chi_1}T_{\chi_2} - \delta^2}}. \quad (\text{A8})$$

where $2m_{\chi_1}T_{\chi_2} > \delta^2$ should be satisfied. The minimum value of E_p^{\min} is $m_p + \delta + \frac{\delta(\delta+2m_p)}{2m_{\chi_1}}$. The condition $E_p > E_p^{\min}(T_{\chi_2})$ is equivalent to $T_{\chi_2}^{\min}(E_p) < T_{\chi_2} < T_{\chi_2}^{\max}(E_p)$.

2. The process in the detector $\chi_1 + N \rightarrow \chi_2 + N'$

For the process $\chi_1(p_1) + N(p_2) \rightarrow \chi_2(p_3) + N'(p_4)$ with $p_2 = (E_2 = m_N, \mathbf{p}_2 \simeq 0)$, we can swap the index that the incoming particle 1 is inelastic DM but E_4 is the energy of the

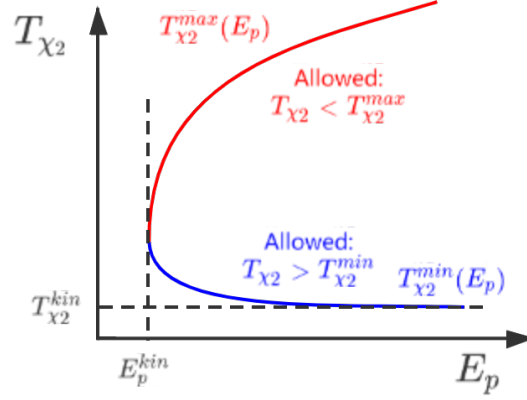


FIG. 10. Kinetic relation between incoming E_p and outgoing T_{χ_2} . From Eq. (A7), the red curve represents $T_{\chi_2}^{max}$ with $\theta^* = \pi$ and the blue curve represents $T_{\chi_2}^{min}$ with $\theta^* = 0$. The kinetic allowed region is between the red and blue curves. The two curve can be described by Eq. (A8) uniformly. Two limits of the curve correspond to two kinematic constraints for inelastic collision: $T_{\chi_2}^{kin} = \frac{\delta^2}{2m_{\chi_1}}$ and $E_p^{kin} = m_p + \delta + \frac{\delta(\delta+2m_p)}{2m_{\chi_1}}$.

heavy nucleus after the collision. By taking the masses $m_2 = m_4 = m_N$, $m_1 = m_{\chi_1}$, and $m_3 = m_{\chi_1} + \delta$, we can rewrite Eq. (A4) as

$$E_4^* = E_{N'}^* = \frac{m_N(m_N + E_\chi) - \delta(\delta/2 + m_{\chi_1})}{M}. \quad (\text{A9})$$

One can simply boost Eq. (A9) from the CM frame to the Lab frame to obtain the recoil energy $Q = E_4 - m_N$ of nucleus. Finally, the minimal kinetic energy required to obtain a specific recoil energy Q is

$$T_\chi^{min} = \frac{Q}{2} - m_{\chi_1} + \frac{\delta(m_{\chi_1} + \delta/2)}{2m_N} + \frac{\sqrt{Q(2m_N + Q)(m_N Q + \delta^2/2)(m_N Q + (2m_{\chi_1} + \delta)^2/2)}}{2m_N Q}. \quad (\text{A10})$$

Appendix B: Scattering Cross Sections

1. The $2 \rightarrow 3$ cross sections

The differential cross section for the inelastic scattering $p(p_1)\chi_1(p_2) \rightarrow p'(k_1)\chi_1(k_2)V(k_3)$ can be represented as

$$d\sigma_{p\chi_1 \rightarrow p'\chi_1 V} = \frac{(2\pi)^4 |\mathcal{M}_{2 \rightarrow 3}|^2}{4\sqrt{(p_1 \cdot p_2)^2 - m_p^2 m_{\chi_1}^2}} d\phi_3(p_1 + p_2; k_1, k_2, k_3), \quad (\text{B1})$$

where $\mathcal{M}_{2 \rightarrow 3}$ is the total scattering amplitude and $\phi_3(p_1 + p_2; k_1, k_2, k_3)$ is the three-body phase space. Assuming that χ_2 is on-shell, we can apply the narrow width approximation for on-shell χ_2 to separate the scattering process to collision and decay part, namely $p\chi_1 \rightarrow p'\chi_2$ and $\chi_2 \rightarrow \chi_1 V$. Therefore, by using the recursive relation, we have

$$d\phi_3(p_1 + p_2; k_1, k_2, k_3) = d\phi_2(p_1 + p_2; k_1, q) \times d\phi_2(q; k_2, k_3) (2\pi)^3 dq^2 \quad (\text{B2})$$

where q is the four-momentum of χ_2 . This kind of technique is extensively used in Ref. [51]. Applying the narrow width approximation for on-shell χ_2 , $|\mathcal{M}_{2 \rightarrow 3}|^2$ will be

$$|\mathcal{M}_{2 \rightarrow 3}|^2 = |\mathcal{M}_{2 \rightarrow 2}|^2 \frac{\pi \delta(q^2 - m_{\chi_2}^2)}{m_{\chi_2} \Gamma_{\chi_2}} |\mathcal{M}_{1 \rightarrow 2}|^2, \quad (\text{B3})$$

where $\mathcal{M}_{2 \rightarrow 2}$ is the scattering amplitude of the collision part and $\mathcal{M}_{1 \rightarrow 2}$ is the one of the decay part.

We can decompose the total differential cross in the following form,

$$d\sigma_{p\chi_1 \rightarrow p'\chi_1 V} = d\sigma_{p\chi_1 \rightarrow p'\chi_2} dB_{\chi_2 \rightarrow \chi_1 V}, \quad (\text{B4})$$

where we have

$$d\sigma_{p\chi_1 \rightarrow p'\chi_2} = \frac{(2\pi)^4 |\mathcal{M}_{2 \rightarrow 2}|^2}{4\sqrt{(p_1 \cdot p_2)^2 - m_p^2 m_{\chi_1}^2}} d\phi_2(p_1 + p_2; k_1, q), \quad (\text{B5})$$

and

$$\begin{aligned} dB_{\chi_2 \rightarrow \chi_1 V} &= \frac{2\pi}{\Gamma_{\chi_2}} \delta(q^2 - m_{\chi_2}^2) \frac{|\mathcal{M}_{1 \rightarrow 2}|^2}{2m_{\chi_2}} d\phi_2(q; k_2, k_3) (2\pi)^3 dq^2 \\ &= \frac{d\Gamma_{\chi_2 \rightarrow \chi_1 V}}{\Gamma_{\chi_2}} \delta(q^2 - m_{\chi_2}^2) dq^2. \end{aligned} \quad (\text{B6})$$

The total width of χ_2 is defined as Γ_{χ_2} .

Finally, we successfully obtain the total differential cross section as Eq. (17),

$$\frac{d\sigma_{p\chi_1 \rightarrow p'\chi_1 V}}{dT_{\chi_1}} = \int \frac{d\sigma_{p\chi_1 \rightarrow p'\chi_2}}{dT_{\chi_2}} \frac{dT_{\chi_2}}{dT_{\chi_1}} \frac{dB_{\chi_2 \rightarrow \chi_1 V}}{d\cos\theta'} d\cos\theta', \quad (\text{B7})$$

where θ' is the angle of χ_1 in the χ_2 rest frame. In this frame:

$$\frac{d\Gamma_{\chi_2 \rightarrow \chi_1 V}}{d\Omega'} = \frac{|p_{\chi_1}^*|}{32\pi^2 q^2} |\mathcal{M}_{1 \rightarrow 2}|^2 \quad (\text{B8})$$

where Ω' is the solid angle. In the presence of vector and axial vector interactions, one can prove that $|\mathcal{M}_{1 \rightarrow 2}|^2$ is independent of the angle. Then the aforementioned θ' can be chosen as the angle formed by χ_2 momentum in the lab frame of p_{χ_1} and χ_1 momentum for $\chi_2 \rightarrow \chi_1 V$ decay in χ_2 rest frame. Therefore

$$dB_{\chi_2 \rightarrow \chi_1 V} = \frac{d\Gamma_{\chi_2 \rightarrow \chi_1 V}}{\int d\Gamma_{\chi_2 \rightarrow \chi_1 V}} \delta(q^2 - m_{\chi_2}^2) dq^2 \longrightarrow \frac{d\Omega'}{4\pi} \quad (\text{B9})$$

At the end, the factor of $\delta(q^2 - m_{\chi_2}^2) dq^2$ will drop out in the process of integration over the three-body phase space [52, 53]. A trivial integration over $d\phi'$ gives the $dB_{\chi_2 \rightarrow \chi_1 V}/d\cos\theta' = 1/2$.

2. The $2 \rightarrow 2$ cross sections

a. The accelerating process $p + \chi_1 \rightarrow p' + \chi_2$

To calculate the total differential cross section between cosmic ray proton and inelastic dark matter in Eq. (B7), we need to derive $d\sigma_{p\chi_1 \rightarrow p'\chi_2}/dT_{\chi_2}$ at first.

$$\frac{d\sigma_{p\chi_1 \rightarrow p'\chi_2}}{dT_{\chi_2}} = \frac{d\sigma_{p\chi_1 \rightarrow p'\chi_2}}{dt} \left| \frac{dt}{dT_{\chi_2}} \right| = \frac{|\overline{\mathcal{M}}|^2}{16\pi\lambda(s, m_p^2, m_{\chi_1}^2)} \left| \frac{dt}{dT_{\chi_2}} \right| \quad (\text{B10})$$

where $|\overline{\mathcal{M}}|^2 = \sum_{spins} |\mathcal{M}|^2/4$ is the proton-DM scattering matrix element squared, averaged over initial spins and summed over final ones. We define the Kallen function as $\lambda(x, y, z) = (x - y - z)^2 - 4yz$ and Mandelstam variables are

$$\begin{aligned} s &= m_{\chi_1}^2 + m_p^2 + 2m_{\chi_1} E_p, \\ t &= -2m_{\chi_1} T_{\chi_2} + \delta^2, \\ u &= m_p^2 + m_{\chi_1}^2 - 2m_{\chi_1} (E_p - T_{\chi_2} - \delta). \end{aligned} \quad (\text{B11})$$

The amplitude squared $|\mathcal{M}_{ij}|^2$ with i for VNN interaction type and j for $V\chi\chi$ interaction type are given in below.

For fermionic DM:

- Vector-Vector interaction:

$$\begin{aligned} |\overline{\mathcal{M}_{VV}}|^2 = & \left[\frac{4(C_N^v)^2(C_\chi^v)^2 m_{\chi_1}}{(2m_{\chi_1} T_{\chi_2} + m_V^2 - \delta^2)^2} \right] \times \left[-4m_{\chi_1} E_p (\delta + T_{\chi_2}) + 4m_{\chi_1} E_p^2 \right. \\ & \left. - 2T_{\chi_2} (m_p^2 + m_{\chi_1} (m_{\chi_1} - T_{\chi_2})) + \delta^2 (m_{\chi_1} - T_{\chi_2}) \right]. \end{aligned} \quad (\text{B12})$$

- Axial vector-Axial vector interaction:

$$\begin{aligned} |\overline{\mathcal{M}_{AA}}|^2 = & \left[\frac{4(C_N^a)^2(C_\chi^a)^2 m_{\chi_1}}{(2m_{\chi_1} T_{\chi_2} + m_V^2 - \delta^2)^2} \right] \times \left[-4m_{\chi_1} E_p (\delta + T_{\chi_2}) + 4m_{\chi_1} E_p^2 \right. \\ & + 2m_p^2 (4\delta + T_{\chi_2}) + 8m_p^2 m_{\chi_1} + m_{\chi_1} (-\delta^2 + 4\delta T_{\chi_2} + 2T_{\chi_2}^2) \\ & + 2m_{\chi_1}^2 T_{\chi_2} + \delta^2 (- (2\delta + T_{\chi_2})) \\ & \left. + (2m_p^2 T_{\chi_2} (\delta + 2m_{\chi_1})^2 (-\delta^2 + 2m_{\chi_1} T_{\chi_2} + 2m_V^2)) / m_V^4 \right]. \end{aligned} \quad (\text{B13})$$

- Vector-Magnetic Dipole interaction:

$$\begin{aligned} |\overline{\mathcal{M}_{MD}}|^2 = & \left[\frac{4(C_N^v)^2 m_{\chi_1} / (\Lambda_M)^2}{(2m_{\chi_1} T_{\chi_2} + m_V^2 - \delta^2)^2} \right] \times 4 \left[4m_{\chi_1} E_p^2 (2m_{\chi_1} T_{\chi_2} - \delta^2) \right. \\ & - 4m_{\chi_1} E_p (\delta + T_{\chi_2}) (2m_{\chi_1} T_{\chi_2} - \delta^2) \\ & - 2m_p^2 T_{\chi_2} (\delta + 2m_{\chi_1})^2 + (2m_{\chi_1} T_{\chi_2} - \delta^2) \\ & \left. \times (\delta^2 (m_{\chi_1} + T_{\chi_2}) + 4\delta m_{\chi_1} T_{\chi_2} + 2m_{\chi_1}^2 T_{\chi_2}) \right]. \end{aligned} \quad (\text{B14})$$

- Vector-Electric Dipole interaction:

$$\begin{aligned} |\overline{\mathcal{M}_{ED}}|^2 = & \left[\frac{4(C_N^v)^2 m_{\chi_1} / (\Lambda_E)^2}{(2m_{\chi_1} T_{\chi_2} + m_V^2 - \delta^2)^2} \right] \times 4 \left[4m_{\chi_1} E_p^2 (2m_{\chi_1} T_{\chi_2} - \delta^2) \right. \\ & - 4m_{\chi_1} E_p (\delta + T_{\chi_2}) (2m_{\chi_1} T_{\chi_2} - \delta^2) \\ & - \delta^2 m_{\chi_1} (3\delta^2 + 4m_p^2 - 4\delta T_{\chi_2} - 2T_{\chi_2}^2) \\ & \left. - \delta^2 (\delta^2 + 2m_p^2) (2\delta + T_{\chi_2}) + 8\delta^2 m_{\chi_1}^2 T_{\chi_2} - 4m_{\chi_1}^3 T_{\chi_2}^2 \right]. \end{aligned} \quad (\text{B15})$$

For scalar DM:

- Combining the vector interaction for SM and \mathcal{L}_1^s in Eq. (4) for scalar DM,

$$\begin{aligned} |\overline{\mathcal{M}}|^2 = & \left[\frac{4(C_N^v)^2 (g_\chi)^2 m_{\chi_1}}{(2m_{\chi_1} T_{\chi_2} + m_V^2 - \delta^2)^2} \right] \\ & \times \left[m_{\chi_1} (4E_p^2 + \delta^2 - 4E_p (\delta + T_{\chi_2}) - 2m_{\chi_1} T_{\chi_2}) \right]. \end{aligned} \quad (\text{B16})$$

- Combining the vector interaction for SM and \mathcal{L}_2^s in Eq. (5) for scalar DM,

$$\begin{aligned} \overline{|\mathcal{M}|^2} &= \left[\frac{4(C_N^v)^2 m_{\chi_1} / (\Lambda_s)^4}{(2m_{\chi_1} T_{\chi_2} + m_V^2 - \delta^2)^2} \right] \\ &\times \frac{1}{4} \left[m_{\chi_1} (4E_p^2 + \delta^2 - 4E_p (\delta + T_{\chi_2}) - 2m_{\chi_1} T_{\chi_2}) (2m_{\chi_1} T_{\chi_2} - \delta^2)^2 \right] \end{aligned} \quad (\text{B17})$$

The corresponding differential cross section can be written as

$$\frac{d\sigma_{p\chi_1 \rightarrow p'\chi_2}}{dT_{\chi_2}} = \frac{m_{\chi_1}}{8\pi\lambda(s, m_p^2, m_{\chi_1}^2)} \overline{|\mathcal{M}|^2} \quad (\text{B18})$$

b. The process in the detector $\chi_1 + N \rightarrow \chi_2 + N'$

In a similar manner, we can derive $d\sigma_{\chi N}/dQ$ of Eq. (21). To calculate $\overline{|\mathcal{M}|^2}$, we only have to change the Mandelstam variables as

$$\begin{aligned} s &= m_{\chi_1}^2 + m_N^2 + 2m_N(T_{\chi_1} + m_{\chi_1}), \\ t &= -2m_N Q, \\ u &= (m_N - m_{\chi_1})^2 + 2m_N(Q - T_{\chi_1}) + \delta(2m_{\chi_1} + \delta). \end{aligned} \quad (\text{B19})$$

The amplitude squared $|\mathcal{M}_{ij}|^2$ with i for Vpp interaction type and j for $V\chi\chi$ interaction type are given in the below.

For fermionic DM:

- Vector-Vector interaction:

$$\begin{aligned} \overline{|\mathcal{M}_{VV}|^2} &= \left[\frac{4(C_N^v)^2 (C_\chi^v)^2 m_N}{(2Qm_N + m_V^2)^2} \right] \times \left[m_N (-\delta^2 - 4(m_{\chi_1} + T_{\chi_1})(-m_{\chi_1} + Q - T_{\chi_1}) + 2Q^2) \right. \\ &\quad \left. - 2Qm_N^2 - 2m_{\chi_1}(\delta^2 + m_{\chi_1}(2\delta + Q)) - 2\delta T_{\chi_1}(\delta + 2m_{\chi_1}) + \delta^2 Q \right] \end{aligned} \quad (\text{B20})$$

- Axial vector-Axial vector interaction:

$$\begin{aligned} \overline{|\mathcal{M}_{AA}|^2} &= \left[\frac{4(C_N^a)^2 (C_\chi^a)^2 m_N}{(2Qm_N + m_V^2)^2} \right] \\ &\times \left[m_N (\delta^2 + m_{\chi_1} (8\delta - 4Q + 8T_{\chi_1}) + 12m_{\chi_1}^2 + 2Q^2 + 4T_{\chi_1} (T_{\chi_1} - Q)) \right. \\ &\quad + 2Qm_N^2 + 2m_{\chi_1}^2 (Q - 2\delta) - 2\delta m_{\chi_1} (\delta - 2Q + 2T_{\chi_1}) + \delta^2 (Q - 2T_{\chi_1}) \\ &\quad \left. + (2m_N (\delta + 2m_{\chi_1})^2 (2Q^2 m_N^2 + Qm_N (\delta^2 + 2m_V^2) + \delta^2 m_V^2)) / m_V^4 \right] \end{aligned} \quad (\text{B21})$$

- Vector-Magnetic Dipole interaction:

$$\begin{aligned} |\overline{\mathcal{M}}_{\text{MD}}|^2 = & \left[\frac{4(C_N^v)^2 m_N / (\Lambda_M)^2}{(2Qm_N + m_V^2)^2} \right] \times 4 \left[4m_N m_{\chi_1}^2 (-\delta^2 + Q^2 - 2\delta Q) \right. \\ & - \delta^2 m_N (\delta^2 - 2Q^2 + 4QT_{\chi_1}) - 4\delta m_N m_{\chi_1} (\delta^2 - 2Q^2 + \delta Q + 2QT_{\chi_1}) \\ & \left. + \delta^2 Q (\delta + 2m_{\chi_1})^2 - 2Qm_N^2 (\delta^2 + 4m_{\chi_1} (\delta + Q - 2T_{\chi_1}) + 4QT_{\chi_1} - 4T_{\chi_1}^2) \right]. \end{aligned} \quad (\text{B22})$$

- Vector-Electric Dipole interaction:

$$\begin{aligned} |\overline{\mathcal{M}}_{\text{ED}}|^2 = & \left[\frac{4(C_N^v)^2 m_N / (\Lambda_E)^2}{(2Qm_N + m_V^2)^2} \right] \times 4 \left[-\delta^2 m_N (\delta^2 - 2Q^2 + 4QT_{\chi_1}) - 4m_N m_{\chi_1}^2 (\delta + Q)^2 \right. \\ & - 4\delta m_N m_{\chi_1} (\delta^2 + \delta Q + 2QT_{\chi_1}) + \delta^2 Q (\delta + 2m_{\chi_1})^2 \\ & \left. - 2Qm_N^2 (\delta^2 + 4m_{\chi_1} (Q - 2T_{\chi_1}) - 4m_{\chi_1}^2 + 4QT_{\chi_1} - 4T_{\chi_1}^2) \right]. \end{aligned} \quad (\text{B23})$$

For scalar DM:

- Combining the vector interaction for SM and \mathcal{L}_1^s in Eq. (4) for scalar DM,

$$\begin{aligned} |\overline{\mathcal{M}}|^2 = & \left[\frac{4(C_N^v)^2 (g_\chi)^2 m_N}{(2Qm_N + m_V^2)^2} \right] \times 2 \left[m_{\chi_1}^2 (-2\delta + 2m_N - Q) \right. \\ & \left. + m_{\chi_1} (-\delta^2 - 2Qm_N + 2T_{\chi_1} (2m_N - \delta)) + T_{\chi_1} (2m_N (T_{\chi_1} - Q) - \delta^2) \right]. \end{aligned} \quad (\text{B24})$$

- Combining the vector interaction for SM and \mathcal{L}_2^s in Eq. (5) for scalar DM,

$$\begin{aligned} |\overline{\mathcal{M}}|^2 = & \left[\frac{4(C_N^v)^2 m_N / (\Lambda_s)^4}{(2Qm_N + m_V^2)^2} \right] \times 2Q^2 m_N^2 \left[2m_N (m_{\chi_1} + T_{\chi_1}) (m_{\chi_1} - Q + T_{\chi_1}) \right. \\ & \left. - m_{\chi_1}^2 (2\delta + Q) - \delta m_{\chi_1} (\delta + 2T_{\chi_1}) - \delta^2 T_{\chi_1} \right]. \end{aligned} \quad (\text{B25})$$

Again, the corresponding differential cross section is

$$\frac{d\sigma_{\chi N}}{dQ} = \frac{m_N}{8\pi\lambda(s, m_{\chi_1}^2, m_N^2)} |\overline{\mathcal{M}}|^2. \quad (\text{B26})$$

[1] Y. Akrami *et al.* [Planck], *Astron. Astrophys.* **641** (2020), A10 doi:10.1051/0004-6361/201833887 [arXiv:1807.06211 [astro-ph.CO]].

- [2] G. Aad *et al.* [ATLAS], [arXiv:2108.13391 [hep-ex]].
- [3] A. Tumasyan *et al.* [CMS], [arXiv:2107.13021 [hep-ex]].
- [4] E. Aprile *et al.* [XENON], Phys. Rev. Lett. **121** (2018) no.11, 111302 doi:10.1103/PhysRevLett.121.111302 [arXiv:1805.12562 [astro-ph.CO]].
- [5] Y. Meng *et al.* [PandaX-4T], [arXiv:2107.13438 [hep-ex]].
- [6] K. Griest and D. Seckel, Phys. Rev. D **43**, 3191-3203 (1991) doi:10.1103/PhysRevD.43.3191
- [7] J. Edsjo and P. Gondolo, Phys. Rev. D **56** (1997), 1879-1894 doi:10.1103/PhysRevD.56.1879 [arXiv:hep-ph/9704361 [hep-ph]].
- [8] H. Baer, T. Krupovnickas, A. Mustafayev, E. K. Park, S. Profumo and X. Tata, JHEP **12** (2005), 011 doi:10.1088/1126-6708/2005/12/011 [arXiv:hep-ph/0511034 [hep-ph]].
- [9] C. Cheung, L. J. Hall, D. Pinner and J. T. Ruderman, JHEP **05** (2013), 100 doi:10.1007/JHEP05(2013)100 [arXiv:1211.4873 [hep-ph]].
- [10] N. Nagata, H. Otono and S. Shirai, JHEP **10** (2015), 086 doi:10.1007/JHEP10(2015)086 [arXiv:1506.08206 [hep-ph]].
- [11] S. Banerjee, S. Matsumoto, K. Mukaida and Y. L. S. Tsai, JHEP **11** (2016), 070 doi:10.1007/JHEP11(2016)070 [arXiv:1603.07387 [hep-ph]].
- [12] Y. L. S. Tsai, V. Tran and C. T. Lu, JHEP **06** (2020), 033 doi:10.1007/JHEP06(2020)033 [arXiv:1912.08875 [hep-ph]].
- [13] K. Cheung, Y. L. S. Tsai, P. Y. Tseng, T. C. Yuan and A. Zee, JCAP **10** (2012), 042 doi:10.1088/1475-7516/2012/10/042 [arXiv:1207.4930 [hep-ph]].
- [14] J. M. Cline, K. Kainulainen, P. Scott and C. Weniger, Phys. Rev. D **88** (2013), 055025 [erratum: Phys. Rev. D **92** (2015) no.3, 039906] doi:10.1103/PhysRevD.88.055025 [arXiv:1306.4710 [hep-ph]].
- [15] T. Lin, E. W. Kolb and L. T. Wang, Phys. Rev. D **88** (2013) no.6, 063510 doi:10.1103/PhysRevD.88.063510 [arXiv:1303.6638 [hep-ph]].
- [16] P. Athron *et al.* [GAMBIT], Eur. Phys. J. C **77** (2017) no.8, 568 doi:10.1140/epjc/s10052-017-5113-1 [arXiv:1705.07931 [hep-ph]].
- [17] S. Matsumoto, Y. L. S. Tsai and P. Y. Tseng, JHEP **07** (2019), 050 doi:10.1007/JHEP07(2019)050 [arXiv:1811.03292 [hep-ph]].
- [18] G. Arcadi, A. Djouadi and M. Raidal, Phys. Rept. **842** (2020), 1-180 doi:10.1016/j.physrep.2019.11.003 [arXiv:1903.03616 [hep-ph]].

- [19] D. S. Akerib *et al.* [LUX], Phys. Rev. Lett. **118** (2017) no.2, 021303 doi:10.1103/PhysRevLett.118.021303 [arXiv:1608.07648 [astro-ph.CO]].
- [20] X. Chen *et al.* [PandaX-II], Phys. Rev. D **96** (2017) no.10, 102007 doi:10.1103/PhysRevD.96.102007 [arXiv:1708.05825 [hep-ex]].
- [21] T. Bringmann and M. Pospelov, Phys. Rev. Lett. **122** (2019) no.17, 171801 doi:10.1103/PhysRevLett.122.171801 [arXiv:1810.10543 [hep-ph]].
- [22] Y. Ema, F. Sala and R. Sato, Phys. Rev. Lett. **122** (2019) no.18, 181802 doi:10.1103/PhysRevLett.122.181802 [arXiv:1811.00520 [hep-ph]].
- [23] C. V. Cappiello, K. C. Y. Ng and J. F. Beacom, Phys. Rev. D **99** (2019) no.6, 063004 doi:10.1103/PhysRevD.99.063004 [arXiv:1810.07705 [hep-ph]].
- [24] C. V. Cappiello and J. F. Beacom, Phys. Rev. D **100** (2019) no.10, 103011 [erratum: Phys. Rev. D **104** (2021) no.6, 069901] doi:10.1103/PhysRevD.104.069901 [arXiv:1906.11283 [hep-ph]].
- [25] G. Guo, Y. L. S. Tsai and M. R. Wu, JCAP **10** (2020), 049 doi:10.1088/1475-7516/2020/10/049 [arXiv:2004.03161 [astro-ph.HE]].
- [26] S. F. Ge, J. Liu, Q. Yuan and N. Zhou, Phys. Rev. Lett. **126** (2021) no.9, 091804 doi:10.1103/PhysRevLett.126.091804 [arXiv:2005.09480 [hep-ph]].
- [27] G. Guo, Y. L. S. Tsai, M. R. Wu and Q. Yuan, Phys. Rev. D **102** (2020) no.10, 103004 doi:10.1103/PhysRevD.102.103004 [arXiv:2008.12137 [astro-ph.HE]].
- [28] N. F. Bell, J. B. Dent, B. Dutta, S. Ghosh, J. Kumar, J. L. Newstead and I. M. Shoemaker, [arXiv:2108.00583 [hep-ph]].
- [29] P. Gallagher, S. Groote and M. Naeem, Particles **3** (2020) no.3, 543-561 doi:10.3390/particles3030037 [arXiv:2001.04106 [hep-ph]].
- [30] M. A. Ivanov, J. G. Körner and C. T. Tran, Phys. Rev. D **92** (2015) no.11, 114022 doi:10.1103/PhysRevD.92.114022 [arXiv:1508.02678 [hep-ph]].
- [31] H. Ruegg and M. Ruiz-Altaba, Int. J. Mod. Phys. A **19** (2004), 3265-3348 doi:10.1142/S0217751X04019755 [arXiv:hep-th/0304245 [hep-th]].
- [32] Z. Liu, Y. Su, Y. L. Sming Tsai, B. Yu and Q. Yuan, JHEP **11** (2017), 024 doi:10.1007/JHEP11(2017)024 [arXiv:1708.04630 [hep-ph]].
- [33] J. D. Lewin and P. F. Smith, Astropart. Phys. **6** (1996), 87-112 doi:10.1016/S0927-6505(96)00047-3

- [34] A. W. Strong and I. V. Moskalenko, *Astrophys. J.* **509** (1998), 212-228 doi:10.1086/306470 [arXiv:astro-ph/9807150 [astro-ph]].
- [35] M. J. Boschini, S. Della Torre, M. Gervasi, D. Grandi, G. Jóhannesson, M. Kachelriess, G. La Vacca, N. Masi, I. V. Moskalenko and E. Orlando, *et al.* *Astrophys. J.* **840** (2017) no.2, 115 doi:10.3847/1538-4357/aa6e4f [arXiv:1704.06337 [astro-ph.HE]].
- [36] P. A. Zyla *et al.* [Particle Data Group], *PTEP* **2020** (2020) no.8, 083C01 doi:10.1093/ptep/ptaa104
- [37] K. Bondarenko, A. Boyarsky, T. Bringmann, M. Hufnagel, K. Schmidt-Hoberg and A. Sokolenko, *JHEP* **03** (2020), 118 doi:10.1007/JHEP03(2020)118 [arXiv:1909.08632 [hep-ph]].
- [38] A. L. Fitzpatrick, W. Haxton, E. Katz, N. Lubbers and Y. Xu, *JCAP* **02** (2013), 004 doi:10.1088/1475-7516/2013/02/004 [arXiv:1203.3542 [hep-ph]].
- [39] A. L. Fitzpatrick, W. Haxton, E. Katz, N. Lubbers and Y. Xu, [arXiv:1211.2818 [hep-ph]].
- [40] N. Anand, A. L. Fitzpatrick and W. C. Haxton, *Phys. Rev. C* **89** (2014) no.6, 065501 doi:10.1103/PhysRevC.89.065501 [arXiv:1308.6288 [hep-ph]].
- [41] F. Bishara, J. Brod, B. Grinstein and J. Zupan, *JCAP* **02** (2017), 009 doi:10.1088/1475-7516/2017/02/009 [arXiv:1611.00368 [hep-ph]].
- [42] F. Bishara, J. Brod, B. Grinstein and J. Zupan, [arXiv:1708.02678 [hep-ph]].
- [43] <https://indico.icranet.org/event/1/contributions/37/attachments/310/378/PandaX-4T-1st-release-MG16-7-8-2021.pdf>
- [44] R. Barbieri and T. E. O. Ericson, *Phys. Lett. B* **57**, 270-272 (1975) doi:10.1016/0370-2693(75)90073-8
- [45] H. Leeb and J. Schmiedmayer, *Phys. Rev. Lett.* **68**, 1472-1475 (1992) doi:10.1103/PhysRevLett.68.1472
- [46] E. Izaguirre, G. Krnjaic and B. Shuve, *Phys. Rev. D* **93**, no.6, 063523 (2016) doi:10.1103/PhysRevD.93.063523 [arXiv:1508.03050 [hep-ph]].
- [47] A. Berlin and F. Kling, *Phys. Rev. D* **99**, no.1, 015021 (2019) doi:10.1103/PhysRevD.99.015021 [arXiv:1810.01879 [hep-ph]].
- [48] D. W. Kang, P. Ko and C. T. Lu, *JHEP* **04**, 269 (2021) doi:10.1007/JHEP04(2021)269 [arXiv:2101.02503 [hep-ph]].
- [49] A. Aranda and C. D. Carone, *Phys. Lett. B* **443**, 352-358 (1998) doi:10.1016/S0370-

- 2693(98)01309-4 [arXiv:hep-ph/9809522 [hep-ph]].
- [50] S. Tulin, Phys. Rev. D **89**, no.11, 114008 (2014) doi:10.1103/PhysRevD.89.114008 [arXiv:1404.4370 [hep-ph]].
- [51] X. W. Kang and J. A. Oller, Eur. Phys. J. C **77**, no.6, 399 (2017) doi:10.1140/epjc/s10052-017-4961-z [arXiv:1612.08420 [hep-ph]].
- [52] X. W. Kang, B. Kubis, C. Hanhart and U. G. Meißner, Phys. Rev. D **89**, 053015 (2014) doi:10.1103/PhysRevD.89.053015 [arXiv:1312.1193 [hep-ph]].
- [53] L. Zhang, X. W. Kang, X. H. Guo, L. Y. Dai, T. Luo and C. Wang, JHEP **02**, 179 (2021) doi:10.1007/JHEP02(2021)179 [arXiv:2012.04417 [hep-ph]].